Universitat Autònoma de Barcelona

EGNITE: Engineered Graphene for Neural Interface

Damià Viana Casals

EGNITE

Engineered Graphene for Neural Interface

by

Damià Viana Casals

PhD thesis approved in its confidential version by signatories below:

Damià Viana Casals

Author

Prof. Dr. Jose Antonio Garrido Ariza

Director

EGNITE

Engineered Graphene for Neural Interface

Damià Viana Casals

PhD Thesis in
Electronic Engineering and
Telecommunications

ICN2 EXCELENCIA SEVERO OCHOA
Institut Català de Nanociència i Nanotecnologia

Supervised by
Jose Antonio Garrido

October 2020

UAB
Universitat Autònoma de Barcelona

I confirm that this PhD Thesis is my own work and I have documented all sources and material used.

Barcelona, 10 October 2020 Damià Viana Casals

Abstract

Neural implants technology in medicine aims to restore nervous system functionality in cases of severe degeneration or damage by recording or stimulating the electrical activity of the nervous tissue. Currently available neural implants offer a modest clinical efficacy partly due to the limitations posed by the metals used at the electrical interface with the tissue. Such materials compromise interfacing resolution, and therefore functional restoration, with performance and stability. In this work, we present flexible neural implants based on a biocompatible nanostructured porous graphene thin film that provides a stable and high performance bidirectional neural interface. Compared to standard platinum microelectrode devices, the graphene-based electrodes of 25 μm diameter offer significantly lower impedance and can safely inject 200 times more charge for more than 100 million pulses. We assessed their performance in vivo by recording high fidelity and high resolution epicortical activity, by stimulating subsets of axons within the sciatic nerve with low thresholds and high selectivity and by modulating the retinal activity with high precision. The graphene thin film technology we describe here has the potential to become the new performance benchmark for the next generation of neural implant technology.

Acknowledgements

When my friend Nico told me in a dinner that the university was offering a course about neural interfaces, I immediately knew it was a path I wanted to follow. At that time, we both were starting a Master's degree in Applied Physics and Engineering at the Technische Universität München after few months of an Erasmus experience there. The day after I went to the class with a curriculum and high expectations to speak with the professor, Jose Antonio Garrido. Almost seven years after, I am presenting a PhD thesis about technology for bidirectional neural interfaces.

I want to acknowledge to all the people I walked together with along the way who helped me make this possible. To Jose Antonio Garrido for the support and the mentoring throughout these years. To Steven Walston for the dedicated work and time we spent together developing many of the results that I am presenting here. To Xavi Illa for the unconditional and essential support in the development of the technology. To Clément Hébert for the counseling and inspiring conversations. To Jaume del Valle, Natalia de la Oliva and Diep Nguyen for the support in the preclinical experiments. To Anton Guimerà for the technical support in the data analysis. To Andrea Bonaccini, Jose Manuel de la Cruz and Eduard Masvidal for the team work. To Nicolás Coca for discovering me such an interesting topic.

I would also like to acknowledge to my sister Marta, my parents Glòria and Amadeu and my partner Cristina for being always by my side.

Table of Contents

List of Figures

1

Introduction

New directions in science are launched by new tools much more often than by new concepts

Imagined Worlds
Freeman Dyson

These are the investigations carried out to develop bidirectional and high resolution neural implants based on graphene. A four-year labor to explore the capabilities of this material to record and stimulate the nervous system with unprecedented accuracy and stability. To seek out new safe and more efficient neuromodulation therapies. To go where no neural implant has gone before [1].

1.1 Towards precise neural interfaces

Modern medicine has focused since the last second half of the 20th century on genetics [2]. The sequencing of the human genome, in the frame of a very ambitious project, the Human Genome Project, became a revolutionary tool to better understand biologic mechanisms in ways that were not possible before [3]. The acquired knowledge, was then invested in improving existing medical therapies and developing new ones.

Now, in the first half of the 21st century, there is a rising interest to study the nervous system, and ultimately, the biology of the brain [4]. Highly ambitious initiatives have been promoted around the world with the goal to reveal the mysteries

of the brain, to improve our understanding of how neural circuitry functions and to develop better treatments for diseases related to the nervous system [5–14]. Similarly as happened with the genome, new tools are being developed to interface with the nervous system with unprecedented accuracy. In the field of neuroscience, these tools should safely and effectively interface with the nervous tissue on a natural way and with minimal invasiveness [15–17].

The organs and functions from our bodies are partially regulated through circuits of neurons communicating through electrical impulses, the action potentials. It is through them that we perceive, act, think, learn, remember and partially regulate organs functioning [4]. Because of the fundamental role action potentials play, their control can be potentially used to diagnose or treat diseases. Neural implants encompass these aspirations [18–21].

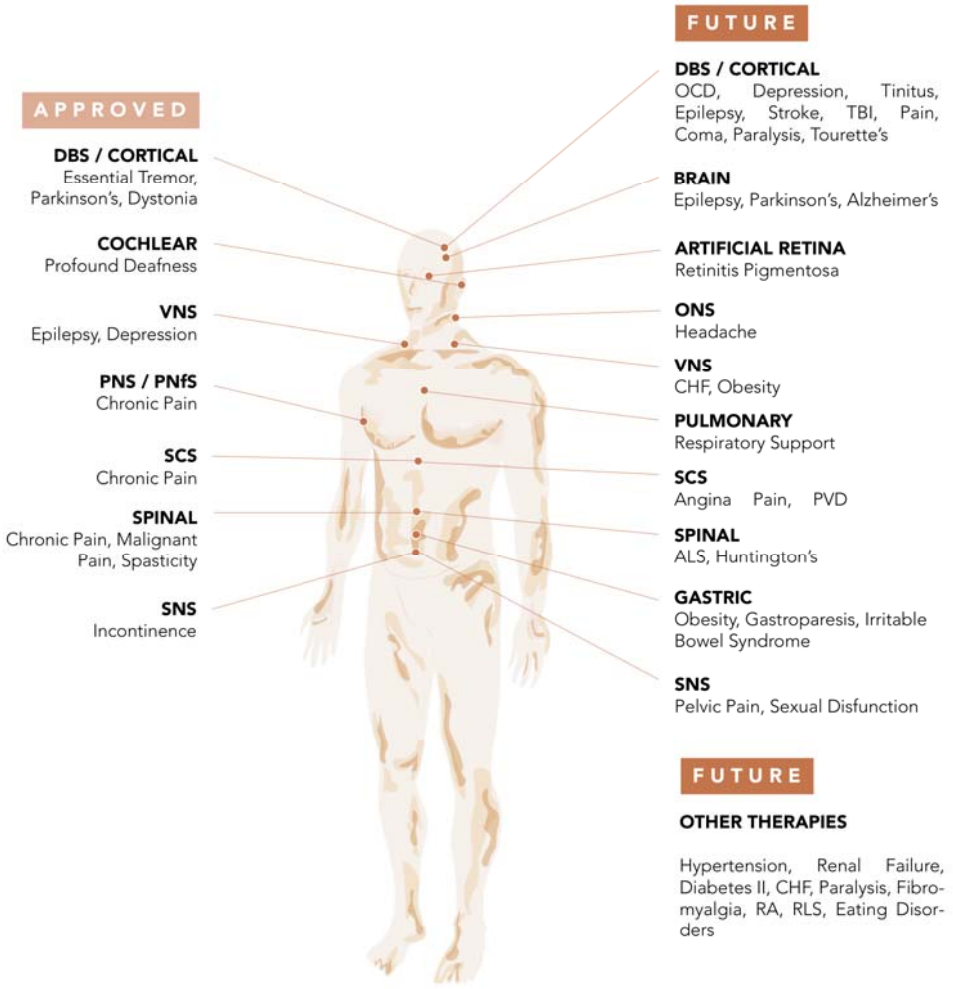

Figure 1.1: Currently approved uses of neuromodulation devices and future prospects, including electroceutical medicine, to treat disorders of the human body. Adapted from [21].

Neural implants technology in medicine aims to restore nervous system functionality in cases of severe degeneration or damage by recording or stimulating the electrical activity of the nervous tissue. To operate, these devices inject electrical current into the tissue in a controlled manner or sense voltage fluctuations from it across neural electrodes [21, 22]. For more than 50 years pacemakers have been used to regulate the electrical conduction system of the heart [21]; cochlear implants to partially restore the hearing sensation [18]; since 1997, deep brain stimulators to treat essential tremor and Parkinson's disease [21]; and more recently, epicortical grids have been used to treat epilepsy and decode intended speech directly from the brain electrical activity [21, 23]. Other neural implants, like retinal implants to restore vision or intraneural interfaces to perceive and move neuroprosthetic limbs, have been explored for a long time but have not reached broad adoption yet because they do not generate naturalistic patterns of action potentials [24–26]. To achieve broader acceptance of such neural implants as a therapy, there is a need for a step-change in improvement of their efficacy and safety so that the benefit of the therapeutic approach outweighs the risks from surgical implantation [26–30].

Recently, researchers and clinicians agreed on the interest to develop electroceutical medicine, a new kind of therapy that could regulate a host of bodily activities. They could, for example, stimulate the production of insulin to treat diabetes, regulate food intake to treat obesity, or modulate specific neural circuits to control inflammation [31]. Such medicine would consist of miniature, implantable devices that attach to individual peripheral nerves and can decipher and modulate neural signalling patterns, achieving therapeutic effects that are targeted at single functions of specific organs. To achieve so, electroceutical medicine would be based on the scientific and technological advances from the last decades in the field of neural interfaces [31–33]. Figure 1.1 shows the neural implants currently approved by the regulatory agencies and the ones envisaged to be developed, together with the associated pathologies to be treated. These days, electroceuticals face some of the challenges retinal implants and intraneural devices encountered for decades, to stimulate neural activity following naturalistic patterns. For that, stimulation with high specificity is required, ideally with resolution close to single neuron [15, 16, 34]. Usually neurons have a soma of 20-30 μm diameter and possess an elongated axon, that can be modelled as cable of about 0.2 μm diameter [4]. Depending on the neural implant, the interface with neurons is aimed to occur with the bodies or the axons, meaning that the stimulation provided by the device should resolve these dimensions. The benefit that such interfaces can provide usually increases

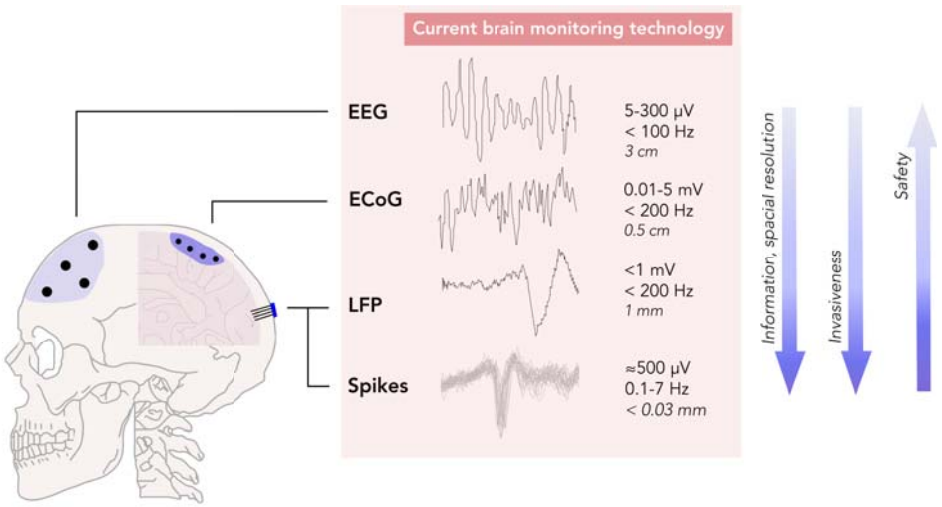

Figure 1.2: Correlation between potential benefit, invasiveness and interfacing resolution of brain monitoring technology. As the electrodes are more invasive, they have greater associated risk. However, the greater invasiveness and precision correlates with a potentially more intimate interface with the nervous system and potentially greater benefit to the user.

with their invasiveness and resolution [21]. Figure 1.2 illustrates this tendency for brain monitoring technology: by interfacing with higher spatial resolution, more naturalistic action potential patterns can be conveyed and more information can be eventually transmitted between the nervous system and device. For instance, the electroencephalography (EEG) technique places electrodes on the scalp and the neural recordings acquired are usually used to diagnose sleep disorders, depth of anesthesia, coma, encephalopathies and used as a first-line method of tumors and strokes diagnosis [35]. In the electrocorticography (ECoG), the electrodes are placed directly on the brain surface and the recorded data used to localise epileptogenic zones during presurgical planning, map cortical functions and more recently, to decode intended speech [29, 36]. Neural recordings obtained with intracortical devices that penetrate deep inside the brain permit predicting intended movement and fingers pressure to control neuroprosthetic limbs with many degrees of freedom [37]. Thus, the more precise the information the implants record, the devices tend to be more invasive but able to transmit more relevant information, which then can be used for a greater benefit of patients. In the neural stimulation front this tendency is similar, increasing the efficacy and potential benefit of the applied neuromodulation therapies with the spatial resolution of the signals transmitted. However, higher precision usually requires more invasive devices, which have a higher safety risk associated [38].

Current clinical neural electrodes technology is not capable of chronically delivering functional stimulation at single cell resolution, so far it can only modulate large groups of neurons with millimetre-scale precision, which sets a limitation on the benefit these devices can provide [22]. To overcome this limitation, alternative strategies to electrical stimulation, like optogenetics, have been suggested [16, 33]. However, optogenetics still requires implantable transducers and struggles to achieve this resolution, reaching it only at high light intensities, with the risk of tissue damage [39, 40]. Even though optogenetic therapies are currently moving towards clinical trials, we envisage to further develop neural electrodes technology, already widely used in clinics, to achieve chronic stimulation capabilities with resolutions close to single neuron [41, 42].

In the following sections, we discuss neural electrodes and the principles behind their interface with the nervous tissue. We talk about the limits of current technology and the approaches followed so far to try to overcome them. We introduce graphene, a very promising material for neural interface, but with some limitations, specially on the stimulation front. Finally, we present the strategies we followed in this thesis to develop Engineered Graphene for Neural Interface (EGNITE), a material whose interfacing resolution capabilities go beyond the possibilities of current clinical technology.

1.2 Neural electrodes

Electrodes are conductors used to establish electrical contact with nonmetallic parts of a circuit [21]. When an electrode is immersed in a physiological solution, an interface is created between the two phases. In the electrode phase, the charges are carried by electrons, while in the physiological solution, or the electrolyte, the charge is conveyed by dissolved ions like sodium, potassium and chloride [18]. At the electrode/electrolyte interface, charge carriers from electrons in the metal electrode can be transduced to ions in the electrolyte and vice versa. To achieve current flow through the electrolyte, at least two electrodes need to be placed in it. One of the electrodes, the one to be studied, is the working electrode (WE) and the second one, used to close the circuit, is the counter electrode (CE) [43]. To study only half of the electrochemical cell, i.e. the behavior of the interface between the WE and the electrolyte, a third electrode is necessary, namely the reference electrode (RE). Under this configuration, the current flows between the WE and the CE while the potential of the WE is measured with respect to the RE. Thus, the potential is not affected

by the current flowing through the interface between the RE and the electrolyte and the measurements are more stable [43]. In equilibrium conditions, there is no net flux of current flowing between the phases but electrical potential gradients appear at the interfaces, in an attempt to balance the electrochemical potential differences between the phases. In case the equilibrium condition is shifted away, the potential gradient, which now extends to the electrolyte as well, induces a net flow of current caused by the charge transfer mechanisms taking place at the electrode-electrolyte interface.

There are two kind of charge transfer mechanisms: non-Faradaic and Faradaic [22, 43], as illustrated in Figure 1.3. Non-Faradaic or capacitive processes do not have net flow of charges across the interface since they are based only on the redistribution of charged ions in the electrolyte. Faradic processes, on the contrary, imply a net transfer of electrons between the electrode and the electrolyte, causing the reduction or oxidation of chemical species of the electrolyte.

Both mechanisms are processes taking place at the interface between the electrode and the electrolyte. Thus, their contributions to the current linearly scale with the electrochemically active surface area (EASA). This area is usually different from the geometric surface area (GSA), which does not take into account the roughness of the electrode. In the next sections two fundamental parameters for the neural interface will be defined from these charge transfer mechanisms: the interfacial impedance (Z_{int}) and the charge injection limit (CIL).

1.2.1 Capacitive charge transfer

Upon immersing a conductive solid in an electrolyte, an electrical double layer is formed at the interface between the two phases. The charge distribution in the electrolyte phase of this double layer comprises an inner layer of adsorbed water molecules and specifically adsorbed ions, and an outer layer of hydrated ions forming a diffuse layer, as described by the Gouy-Chapman-Stern (GCS) model. The inner layer, also called Helmholtz layer, contributes to the overall double layer capacitance C_{dl} with C_H. The diffusive layer capacitance C_{diff}, with a strong dependence on the electrolyte concentration and electrode potential, adds in series to it:

$$\frac{1}{C_{dl}} = \frac{1}{C_H} + \frac{1}{C_{diff}} \tag{1.1}$$

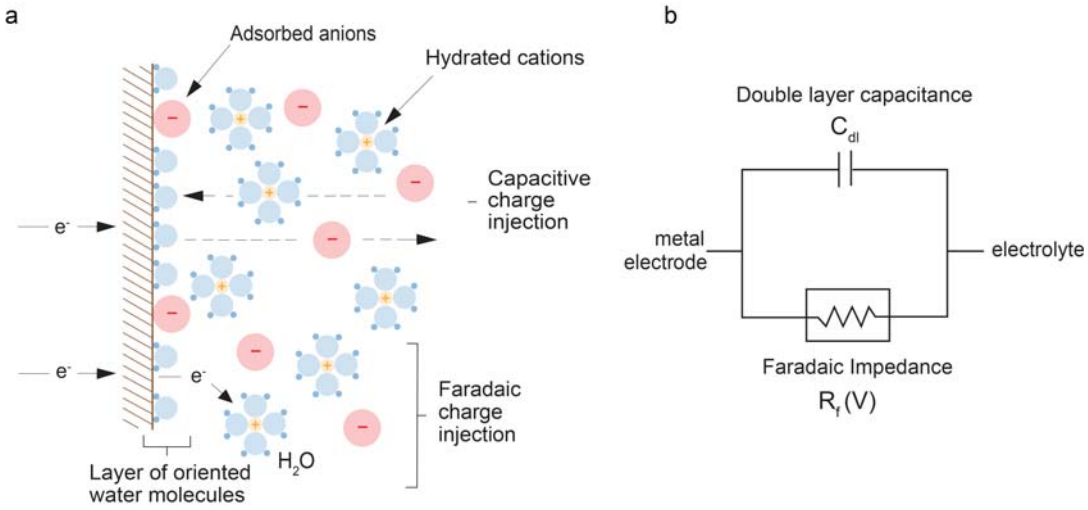

Figure 1.3: Schematic of the electrode/electrolyte interface. **a.** Top. Double layer capacitance in which the charge from the electrode is balanced by ions from the electrolyte specifically adhered to its surface and by a diffusive layer of ions. Upon variations of the electrode charge, the double layer charges and discharges leading to capacitive currents. Bottom. Faradaic processes in which species from the electrolyte exchange electrons with the electrode surface, creating new species and modifying it. Depending on the kinetics of the reactions, the processes might be reversible or irreversible. For neural stimulation purposes, irreversible reactions must be avoided, but reversible ones are tolerated. **b.** Approximated electric equivalent circuit of the electrode/electrolyte interface. The double layer can be modelled as a capacitor and the Faradaic reactions as a voltage dependent resistance. Adapted from [43].

In electrolytes with high ionic concentrations, and close to the equilibrium potential, the double layer highly compacts to tens of Å and the C_{dl} tends to the C_H, which is modelled as a single plane capacitor:

$$C_{dl} \approx C_H = \frac{\varepsilon_0 \varepsilon EASA}{d} \tag{1.2}$$

, where ε_0 and ε are the permitivity of the vacuum and the dielectric constant of the medium, respectively, and d is the interplate spacing, usually with values smaller than 10 Å [43]. An alternative description is:

$$C_{dl} = c_i EASA \tag{1.3}$$

, with c_i being the intrinsic capacitance of the electrode material and already including the electrical double layer features of the interface. Experimental measurements of this magnitude reveal an additional dependence on the applied voltage, which can be explained by the surface electrochemistry of the electrode materials and the behavior of the ions in the electrolyte [43].

Neural stimulation. For neural electrodes, capacitive interfaces are advised in order to ensure the safety of the charge carriers transduction, especially for neural stimulation purposes, as it is explained next. To ensure functionality under those circumstances, these interfaces should be able to inject enough charge to modulate the tissue activity [22].

If the net charge of an electrode in solution is forced to vary, the charge of the electrolyte redistributes to keep the charge neutrality of the interface. To do so, a voltage difference should be applied between the two electrodes immersed in the electrolyte so that current flows between the two across the solution. The electrode driven towards positive potentials will attract anions dissolved in the solution and repel cations. In opposition, the other electrode, forced to negative potentials, will pull cations towards its surface and push away anions. These processes will result in the charge and discharge of the C_{dl} and in a net capacitive current I_c flowing across the interface that can be modelled according to [43]:

$$I_c = C_{dl}\frac{dU}{dt} \tag{1.4}$$

, where dU/dt is the voltage shift across the interface.

The electrical potential range within which the currents remain purely capacitive without involving net transfer of charges through Faradaic reactions is called electrochemical potential window. The involvement of Faradic reactions in neural stimulation processes might harm the tissue and degrade the electrode material, as will be later explained in more detail [22]. In aqueous solutions, the potential window ΔU is limited by electrolysis, which typically varies depending on the electrode material and extends over less than 1 V. Ideally non polarisable or blocking electrodes are those electrodes with purely capacitive interfaces. Under those circumstances, the charge Q that the electrode can store in the double layer and inject into the tissue is:

$$Q = C_{dl}\Delta U \tag{1.5}$$

To prevent tissue overcharging and damage, stimulation protocols consisting of biphasic, charge-balanced and current controlled pulses are usually employed. These protocols can be defined by parameters such as the current amplitude, phase duration and charge injected per phase ($Q/phase$). Values of $Q/phase$ in the range of few tens of $nC/phase$ are usually required for in vivo neural stimulation, as will be later explained [22]. Combining Equation 1.3 and 1.5 it is obvious the linear dependency between Q and the c_i, the EASA and the ΔU. Thus, to inject high amounts of charge

into the tissue, materials with high c_i, large EASA and wide ΔU are good candidates to be used as electrodes.

In real applications however, a more accurate electrical description of the system is given by a model that contains the resistive contributions of electrons to access to the material surface [44, 45]. These resistive components, in combination to the capacitive contributions, set a time-constant to the system. To stimulate the nervous tissue with high precision, not only naturalistic resolution is spatially required, but also temporal resolution in the range of neurons action potentials. To achieve so, the charge should be delivered in times in the range of 1 ms [22].

Neural recording If the charge and discharge of the double layer occurs rapidly, like when recording the neural activity, a better way to display the interface equations is in the frequency domain [18]. Then, Equation 1.4 can be rewritten as:

$$U = I\frac{1}{i\omega C_{dl}} \tag{1.6}$$

, being ω the angular frequency and i the imaginary unit. From Equation 1.6, the impedance of the interface Z_{int} arises to be:

$$Z_{int} = \frac{1}{C_{dl} i\omega} \tag{1.7}$$

In neural recordings, the level of noise of the measurement is primarily given by the root mean square (rms) thermal noise U_{rms} calculated from the Johnson–Nyquist equation [18]:

$$U_{rms} = \sqrt{4KT\Delta(f)Re(Z_{int})} \tag{1.8}$$

, where K is the Boltzmann constant, T the temperature and $\Delta(f)$ the bandwidth of the measurement. In purely capacitive interfaces the noise level is given by non imaginary contributions of the impedance, like connectors, the finite conductivity of the electrode material or possible Faradaic reactions. The double layer capacitance, modelled as pure capacitor, shall not contribute to it. However, for real applications, a more accurate description is given by an equivalent electric circuit that takes into account the access resistance of the electrons to the electrode R_s and considers the electrode as a finite elements volumetric distribution of resistances and capacitances. Additionally to this distribution, surface heterogeneities such as grain boundaries, crystal faces on a polycrystalline electrode can further increase the dispersion of contributions to the current. This complex behavior is commonly simplified and represented in equivalent electrical circuits as constant-phase elements (CPEs) [44].

These, represent general circuit elements that show a constant phase angle dephasing of the current with respect to the voltage. Pure capacitors exhibit an angle of -90^o dephasing, but when replaced by CPEs to better fit experimental data, they can show angles closer to zero and contribute to the impedance with non purely imaginary components. Then, the interfacial impeadance becomes:

$$Z_{int} = \frac{1}{Q_{int}(i\omega)^n} \tag{1.9}$$

, where Q is the value of the CPE and n its ideality with respect to the pure capacitor. The exponent n equals 1 for pure capacitor but can have values closer to zero for less ideal interfaces, such as distributions of resistances and capacitors. Alike C_{dl}, Q_{int} scales with the c_i and the EASA. Thus, to obtain low levels of noise, highly capacitive materials with large EASA are required.

1.2.2 Faradaic charge transfer

Faradaic reactions are charge transfer processes that take place in the interfacial region between the electrode and the solution. Once submerged in the electrolyte, electrodes can act as source or sink of electrons transferred to or from species in the solution, depending on the relative difference between the Fermi level of the electrode and the electrolyte bulk potential [43, 46]. The redox reactions are a combination of an electron donating reaction and an electron accepting reaction [18]. The transfer rate of these reactions depends on the difference between the Fermi level of the electrode and the electrochemical potential of the electrolyte.

A schematic plot of such processes is shown next in Figure 1.4, with the associated reactions. By considering the overall system, the following equation can be written:

$$\mathrm{Ox^S} + \mathrm{ne^{-E}} \rightleftharpoons \mathrm{Red^S} \tag{1.10}$$

, where Ox and Red are oxidised and reduced species dissolved in the solution S and ne^- are amount of electrons transferred from or to the electrode E. Furthermore, an equilibrium potential U_{eq} exists at which the transfer rates of each partial reaction equal and no net current flows. If the potential of the electrode is forced to be driven at U, away from the equilibrium, electrons start to flow and the electrode is said to be polarised. The difference between the electrode potential U and the equilibrium potential U_{eq} give rise to the so called overpotential η, which is a measure of the electrode polarisation, and reactions start to occur. Following the electrical modelling

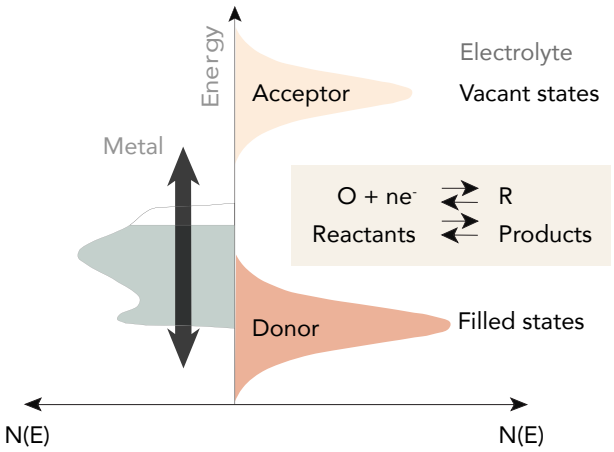

Figure 1.4: Density of states representation of a metal electrode in an electrolyte. The left-hand side corresponds to the metal and the right-hand side represent the density of states for the molecules in the electrolyte. All electron energy states are occupied below the Fermi level in the metal (green) and by the electron donor in the electrolyte (red). As the Fermi level of the electrode rises, no electrons are transferred to the solution until the vacant states level for the acceptor in the electrolyte is reached (yellow). Similarly, when the Fermi level is lowered, electrons are only transferred from the molecules in the electrolyte to the metal when the electron energies are at the same level. Adapted from [21].

of the interface, these contributions can be described by a voltage-gated resistance set in parallel with the double layer capacitance. The Randles circuit shown in Figure 1.3b describes the electrode-electrolyte interface in a very first approximation.

Faradaic reactions are divided into irreversible and reversible reactions [18]. The degree of reversability depends on the relative rates of kinetic and mass transport.

In Faradaic reactions with slow kinetics and large mass transport rates, once formed, the products diffuse away from the surface and cannot be recovered; they are, thus, referred to as irreversible reaction. The charge transfer processes usually take place at η far from the U_{eq} and can lead to the dissolution of the electrode material and change of the pH of the electrolyte, potentially damaging the tissue [18]. Thus, these reactions should be avoided at all costs in neural stimulating electrodes.

On the contrary, reversible Faradaic reaction have a very fast kinetics relative to the rate of mass transport. Since the products of the reactions do not move away from the surface fast enough, by reversing very fast the overpotential, the product that has been just formed can reverse back to its initial condition.

Neural stimulation. Reversible Faradaic processes, when induced by biphasic charge balanced pulses, shall ideally lead to a zero net accumulation of electro-

chemical species; therefore they have similarities with the capacitive stimulation. Analogously to the charge injected by a capacitance, described by Equation 1.5, the pseudocapacitance mechanism describes the introduction of charges into the tissue through reversible Faradaic reactions. This behavior, like in the capacitance, is restricted to the boundaries of the electrode potential window of water. In materials that have pseudocapacitive behavior, like platinum, these contribution adds up to the one from the capacitance. Even though reversible Faradaic reactions are tolerated, their reversibility does not achieve the 100 %. This inevitably leads to the generation of subproducts that could damage the tissue. The charge injection limit (CIL) is described as the maximum charge that can be delivered through capacitive currents or reversible Faradaic reactions without polarising the electrode potential beyond the electrochemical potential window of water. The CIL depends on the electrode material and scales with its EASA. To benchmark the CIL among electrode materials, this magnitude is usually normalised by GSA of the electrode. Upon electrodes miniaturisation, higher values of the CIL are usually required in order to deliver the necessary amount of charge to trigger action potentials.

Neural recording. Neural recordings usually measure voltage fluctuations between few tens of μV to few mV. Thus, at these η, the Faradaic reactions do not play a significant role [22, 43].

1.2.3 Distributed electrical circuit model of the electrode

The Randles circuit from Figure 1.3b is a first approximation model of the electrode-electrolyte interface. However, because its simplicity it is not sufficient to describe the electrochemical behavior observed in many electrodes. For instance, the amount of charge that an electrode can inject is not only constrained by the electrode material, but also by the shape of the electrical stimulus sent through it. Observations indicate that low frequency stimuli permit to inject higher amounts of charge than high frequency signals [22].

To explain this, it is necessary to model the electrode as a distribution of resistive and capacitive elements and to take into account the electrode geometry. Figure 1.5a and b illustrates such the description. There, the intrinsic interfacial capacitance c_i and the voltage dependent Faradaic reactions resistances $R_f(V)$ model the interface between the electrode and the electrolyte, and the intrinsic sheet resistance of the electrode material R_i and the electrolyte resistance $R_{electrolyte}$ are also considered. In the absence of charge transfer induced by Faradaic reactions at the electrode-

electrolyte interface and assuming the electrode material to be much more resitive than the electrolyte, $R_f(V)$ and $R_{electrolyte}$ can be removed leading to a transmission line model with R-C or R-CPE elements distributed along the electrode surface (Figure 1.5c).

Considering a circular electrode with r being the radial distance to the center, the following differential equations can be written to correlate the measured current I with the applied potential U [45]:

$$\frac{dI(r,\omega)}{dr} = Q(i\omega)^n U(r,\omega) \tag{1.11}$$

$$I(r,\omega) = \frac{2\pi r}{R_i}\frac{dU(r,\omega)}{dr} \tag{1.12}$$

, where Q is the value of the CPE, n its exponent, i the imaginary number and ω is the angular frequency of the electrical signal. By solving these equations, the observed dependence of the injected charge on the stimulus frequency phenomenon that could not be explained by the Randles circuit is disclosed. Thus, charge carriers can flow through different paths along the electrode material before charging the distributed capacitor elements and the impedance of each current path corresponds to the impedance of the capacitive element plus the resistance of the electrode from the contact to the corresponding capacitive element. At low frequencies, the impedance of the current paths is dominated by the capacitive elements; thus, all paths contribute equally to the total current and the CIL is maximum. The increase of the signal frequency leads to a reduction of the impedance of the capacitance elements with respect to the resistive paths. As a result, the current paths do not contribute equally to the current. The higher the frequency is, the more relevant this effect gets, and the current will preferentially flow through the paths close to the contact, leading to lower CIL. Thus, to maximise the CIL, the current should flow through as much EASA as possible. To achieve so, the electrical resistivity of the electrode material should be minimised and the interfacial capacitance maximised. This combination is usually achieved by coating highly conductive metallic electrodes with highly capacitive materials [22].

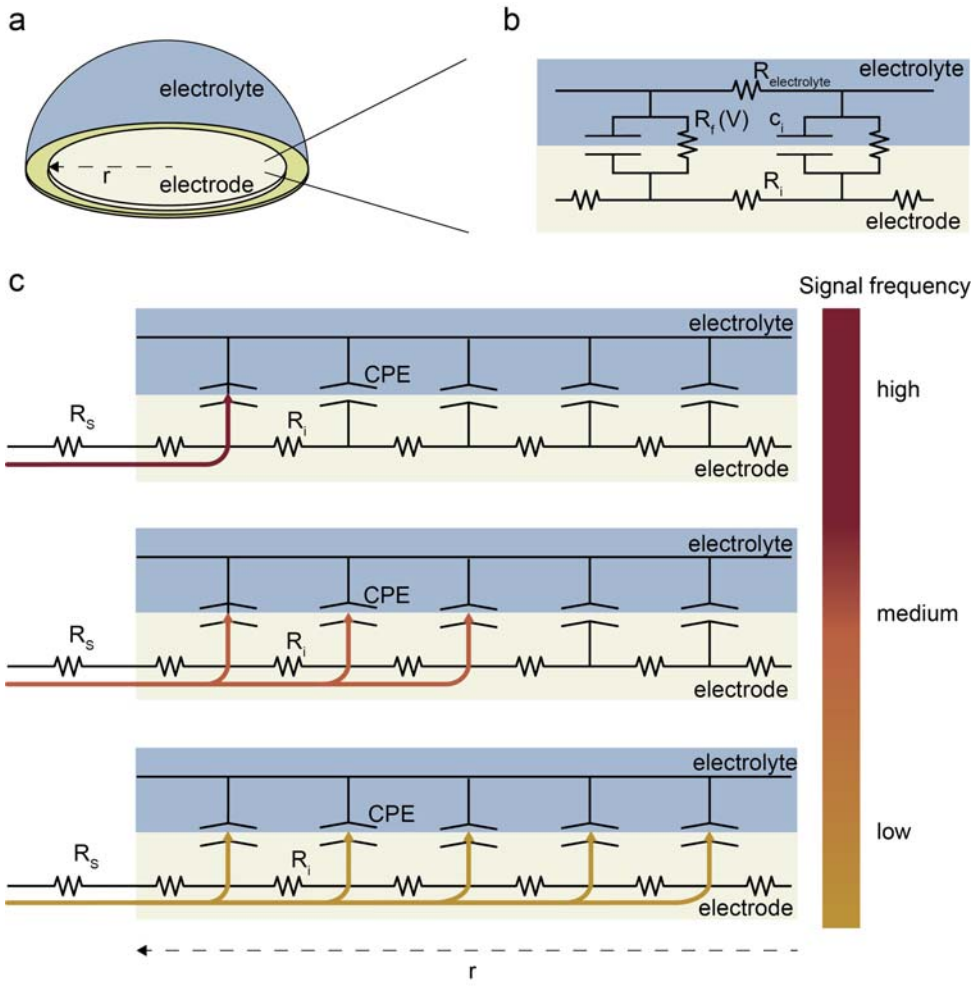

Figure 1.5: Distributed electrical model of the electrodes. **a.** Schematics of the circular electrode. **b.** Distributed elements circuit model describing the electrode-electrolyte interface. R_i is the sheet resistance, c_i represents the interfacial capacitance, $R_f(V)$ is the Faradaic impedance and $R_{electrolyte}$ is the resistance of the solution. **c.** Distributed R-CPE elements modelling a blocking electrode. When an electrical signal is applied between the electrode contact and the electrolyte, the current flows along different paths of the electrode depending on the signal frequency. For low frequency signals all paths contribute equally to the total current and the CIL is maximum. As the signal frequency increases, the farthest paths from the electrode contact no longer contribute to the total flux of current as the impedance of the distributed CPEs increased with respect to the R_i. For high frequency signals, the current flows only through the perimeter of the electrode.

1.2.4 Neural interface constraints upon electrode miniaturisation

To electrically convey naturalistic action potential patterns, the spatial resolution of the interfaces should be able to resolve electrical impulses in the structures of the nervous system responsible for their transmission [15, 26, 31, 47, 48]. As the electrode size is decreased the efficacy of the interface might be compromised. Parameters that directly scale with the electrode surface area, like the interfacial impedance (Z_{int}) and the amount of charge that can be injected into the tissue severely limit the electrodes performance when stimulating and recording the neural activity [22].

Neural stimulation. In the neural stimulation front for example, pacemakers have centimetre-scale metallic electrodes to synchronise the populations of cardiac cells spread few centimetres across the surface of the heart. The particular morphology of the cochlea, separates the processing of the sound along 30 mm [21]. This structure permits to introduce up to 22 platinum electrodes of millimetre-scale to restore the hearing sensation in deaf patients [18]. Deep brain stimulators target to stimulate a centimetre-scale structure in the brain, the basal ganglia. For that, they have several millimetre-scale electrodes, which, again, are made of platinum [21]. To efficaciously interface with finer structures of the nervous system, such as local neuronal circuits or, in the extreme case, individual neurons or their axons, smaller electrodes, ideally in the range of few tens of micrometres, are necessary [15, 26, 31, 47, 48]. The parameters of the electrical pulses used to deliver neuromodulation therapies are derived from the so-called strength-duration curves [49], like the one shown in Figure 1.6a. These curves describe the relationship between the amplitude and duration of a current-controlled pulse to elicit an action potential. The quantitative evaluation of the curve is specific for each kind of neural tissue and depends on the distance between the neurons of interest and the electrode, and the electrode geometry. However common features can be extracted [18, 50–52]. The current required to reach the threshold of the neural activation I_{th}, decreases by increasing the pulse width W. At long pulse widths, the current tends to its minimum, the rheobase current I_{rh}; and these values relate to each other following an experimentally derived equation [50–52]:

$$I_{th} = \frac{I_{rh}}{1 - exp(-W/\tau)} \tag{1.13}$$

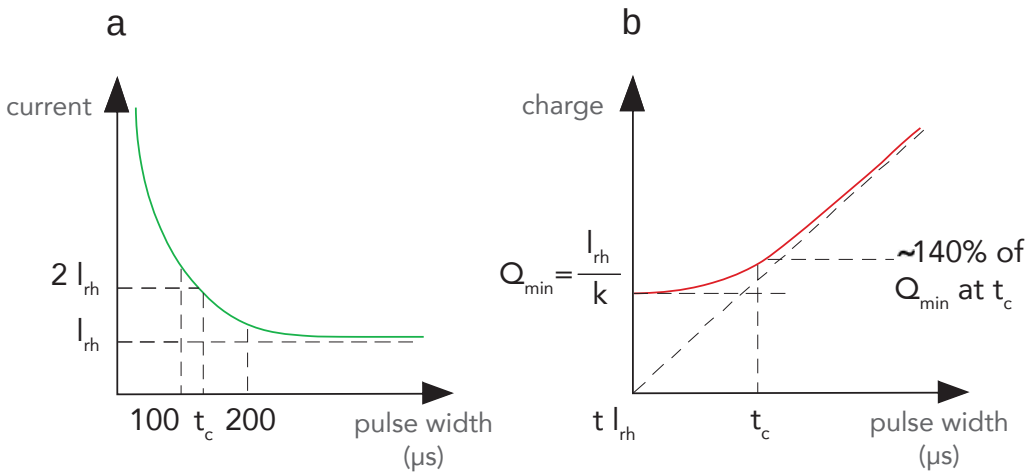

Figure 1.6: Parametric study of single electrical pulses that trigger neural activity. **a.** Strength–duration curve. It defines the threshold parameters of current controlled pulses to trigger an action potential in the nervous tissue. From the plot, two key parameters can be identified: the rheobase I_{rh}, which is the current at infinite duration pulses and the chronaxie, which is the pulse width for threshold currents twice the rheobase. **b.** Charge-duration curve. It has been calculated by integrating a. It determines the amount of current that has to be injected to elicit an action potential.

, where τ is a time constant characteristic for the nerve tissue. For instance, myelinated neurons react about 10 times faster than unmyelinated neurons [53].

The integration of the strength-duration curve leads to the charge-duration curve (Figure 1.6b). From it, it becomes obvious that at longer pulse widths the charge required to elicit a response increases. Two phenomena explain this behavior. First, over few hundreds of μs the charge redistributes along the neuron, so it does not changes that efficiently the transmembrane potential in the site of injection [54, 55]. And second, over these time scales the membrane response of the inactivating sodium channels dominate the dynamics of the transmembrane potential, making more difficult to trigger an action potential [56]. Analogously, the charge required to elicit a response decreases as the pulse width narrows to tens of μs and tends to Q_{min}, the charge in the limit case of 0 s duration pulses [22]. The width of the pulses is usually limited by electronic equipment responsible for the signal generation [57].

In most clinical applications, electrical stimulation is injected through biphasic charge-balanced stimulus waveforms. Neurons from the auditory nerve, the brain and axons in the peripheral nerve system (PNS) need between 5 and 25 $nC/phase$ to be stimulated [61–63]. To confine this amount of charge in microscopic dimensions the electrode sizes have to be at the microscale and thus, the charge density increases to the range of few $mC/(phase \cdot cm^2)$. Clinically used metallic electrodes, such as

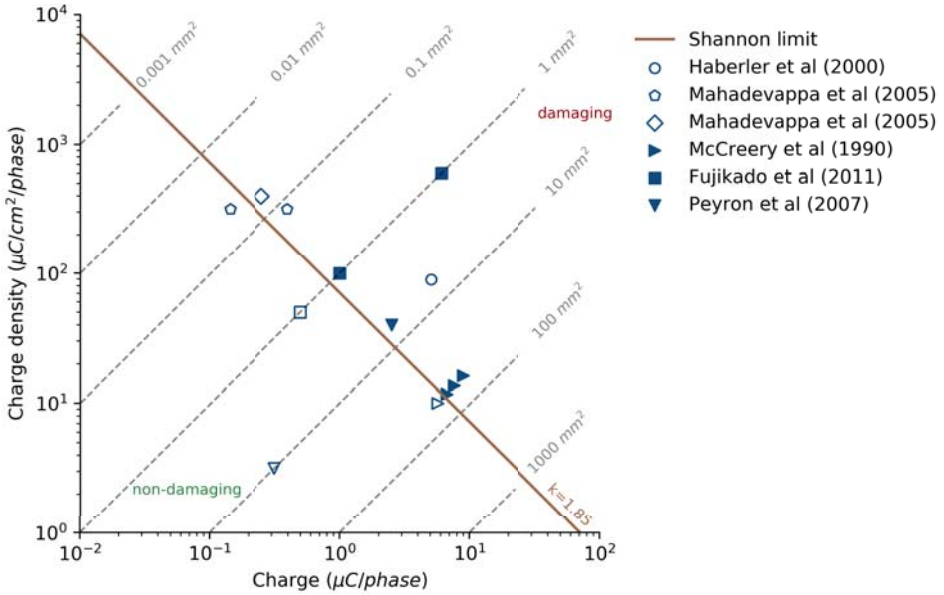

Figure 1.7: Traditional Charge (Q) vs. Charge Density (Q/A) plot to determine the pulse parameters of current controlled pulses to avoid tissue damage during electrical stimulation. According to the Shannon criteria, only parameters below the brown line should be used to stimulate the tissue. These parameters were calculated using histological data from tissue stimulated by macroelectrodes [58]. Recent investigations suggest that the safe regime should be extended when injecting the current with microelectrodes [59, 60].

platinum only offer a CIL of up to 350 $\mu C/(phase \cdot cm^2)$ [64, 65]. To increase such values, new materials are required [66].

Biphasic charge-balanced stimulus waveforms are identified by parameters such as the density of charge per phase D ($\mu C/(phase \cdot cm^2)$) and charge per phase, Q ($\mu C/phase$). In the case of the density, it is computed normalizing the current by the GSA of the electrodes rather then by their EASA, since this is the effective area the current is covering upon injection. Both parameters, D and Q, are correlated with thresholds for tissue damage traditionally described by the Shannon equation [58]:

$$\log D = k - \log Q \tag{1.14}$$

, where k is an adimemensional factor between 1.7 and 1.85. Taking into account the GSA of the electrode, the maximal charge per phase that should be injected to avoid any tissue damage according to equation 1.14, is [22]:

$$Q = \sqrt{GSA * 10^k} \tag{1.15}$$

, which for electrodes of 25 μm of diameter gives Q = 18.8 $nC/phase$ and a maximal D of 3.7 $mC/(phase \cdot cm^2)$. The Shannon equation, however, was derived by considering the effect on the tissue of stimuli elicited by macroscopic scale platinum electrodes [58]. Recent investigations suggest that the safe regime set by Equation 1.14 should be extended when injecting the current with microelectrodes and with alternative materials to platinum [59, 60]. According to such studies, for electrodes smaller than 2000 μm^2 ($\varnothing$ 50 μm) the depression of neuronal excitability was correlated with Q but not D, and the geometric area and shape of the electrode are not significant factors for determining the tissue damage thresholds as long as the irreversible Faradaic reactions do not generate noxious chemical byproducts during stimulation. As a consequence, electrical stimulation performed by small capacitive microelectrodes with CIL in the range of few mC/cm^2 should not damage the neural tissue [59, 60].

Neural recording. Figure 1.2 shows different neural signals of interest labeled depending on their magnitude and relative bandwidth. The synchronous firing of the neurons leads to local field potentials (LFPs), which extend from centimetre to millimetre-scale areas, have amplitudes between few mV and hundreds of μV and last few ms [67]. Individual action potentials last between hundreds of µs to few ms and have an amplitude of tens of mV when measured intracellularly. Extracellularly, their observed amplitude ranges between 500 μV and 20 μV, depending on the electrode location with respect to the firing neurons. In the brain, for instance, intracortical recordings with electrodes densely embedded with the neurons, can register action potential amplitudes of few hundreds of μV [68]. Epicortical devices, located more distally from the neurons, record them with an amplitude of about 40 μV [30]. By increasing the spatial resolution of the recordings, more valuable information can be collected [15]. To do so, the electrode dimensions should be close to the cell size [30, 69]. However, reducing the dimension of the electrodes to such extent significantly reduces the GSA and increases the interfacial impedance, which might have consequences for the neural recordings [22]. The increase of the interfacial impedance (Z_{int}) and the high contribution of its real part translates into noisy recordings with lower signal-to-noise ratio (SNR) [22]. For individual action potentials, the amplitude of interest is between 20 μV and 500 μV [4]. To distinguish the signal from the noise, the first one should be clearly larger than the second one. The relation between the U_{rms} noise, whose main contribution is described in Equation 1.8, and the peak-to-peak amplitude of the recorded signal is of about

8 times [70]. To distinguish 40 μV biological signals, an U_{rms} noise level of 2 μV would be advised [30]. For that, at 37 °C, in a bandwidth between 300 Hz and 3000 Hz, the maximal theoretical value of the real part of the impedance should be 200 kΩ. To minimise the impact of the interfacial impedance on the noise, large EASA electrodes with highly non polarisable behaviors are preferred, like pseudocapacitive interfaces with n factors close to 1 [22]. Apart from the impedance of the interface, other components, like the amplifiers and unpredictable electrochemical fluctuations, introduce electronic noise, but their contribution should be minimal with respect to the one coming from the interface [71].

1.2.5 Towards the ideal electrode material

The ideal material to be used as a neural electrode should satisfy the following requirements. It must be biocompatible, so it should not induce a toxic or necrotic response to the adjacent tissue, nor an excessive foreign body or immune response. The material must maintain its integrity during the implantation period. In case of chronic use, the electrodes should be embedded into flexible devices to withstand small displacements between the tissue and the device after the implantation. The electrode/tissue interface should permit the electrical activity from the tissue to be recorded with high signal-to-noise ratio and that sufficient charge can be injected to it in order to elicit action potentials. Also, the electrode dimensions must accommodate to the morphology of the target nervous tissue, so it can adapt itself to it and convey in an accurate way naturalistic electrical patterns. During electrical stimulation, Faradaic reactions should be avoided to prevent toxicity to the surrounding tissue and electrode corrosion which might lead to premature failure of the interface. Instead, capacitive currents are advised. Finally, the electrical features of the electrode material, such as the impedance and the CIL, should not degrade during the life-time of the implant [22, 72].

Currently, a major limitation of the spatial resolution of clinical neural implants comes from the metallic electrodes used to interface with the nervous tissue, such as platinum (Pt) or iridium (Ir) [22, 73]. While these metallic interfaces can generally offer robust neural signal transduction when used in millimetre-scale electrodes, as electrode size is decreased to the micrometre-scale, their electrical performance dramatically drops, as previously explained. This lowers the SNR during neural recordings and leads to the inability to efficaciously stimulate the nervous tissue.

However, materials like Pt or Ir, have a considerable pseudocapacitive behavior, which reduces the impact of the miniaturisation on neural applications. For instance,

20 μm diameter Pt electrodes have been embedded in intracortical devices to monitor the brain activity with high resolution [74, 75]. Such electrodes, however, are incapable of efficaciously stimulating at such high precision because the amount of charge they can inject is not enough to trigger neural activity [76]. Achieving functional stimulation with Pt would require using large-size electrodes on the millimetre-scale, which sets a constraint in their integration into dense arrays and in the therapeutic benefit they can provide (See Figure 1.2). Furthermore, these large metal electrodes generally increase the rigidity and stiffness of the final devices, limiting their biocompatibility and enhancing fibrotic capsule build-up following implantation [22]. Additionally, the pseudocapacitive behavior still relies on Faradaic reactions that should be avoided, if possible.

To address the inherent neural interfacing resolution and safety problems associated with large metallic electrodes, higher performing and more stable materials have been explored to miniaturise neural interfaces [77]. Surface modification strategies have been investigated to maximise the available EASA while keeping the overall GSA as small as possible. A first approach was to investigate electrodes made of porous metals, which certainly increased the SNR and the CIL. However, their mechanical stability was poor, especially during chronic stimulation, compromising their use for clinical applications [78]. To avoid Faradaic reactions, materials whose interface in aqueous media is capacitive over a wide potential range, such as titanium nitride (TiN), have been tested [79]. However, TiN has been shown to exhibit low biocompatibility in certain cases [80]. As an interesting alternative, conductive polymers (CP), such as poly(3,4-ethylenedioxythiophene) have been suggested in different combinations (PEDOT:PSS or PEDOT-CNT, for instance) due to their large EASA, their capacitive interface and flexibility [81, 82]. However, the stability of these electrodes under continuous stimulation and in chronic applications remains debated [83, 84]. Carbon-based materials fulfill most of the requirements for a neural electrode material. They exhibit a capacitive interface over a wide potential window, they can provide a large EASA and carbon is considered to be biocompatible [85, 86]. It is because of that, that large area carbon derivative materials like carbon nanotubes (CNT), glassy carbon or nanoporous boron-doped diamond have been used for this purpose. All those materials have demonstrated a very good performance for neural interfaces, being able to record with high SNR and capable of injecting relatively high amounts of charge [87–92]. Their acceptance, however, has not been broad. This is because of concerns of different kinds that arouse during the last years regarding the distinct configurations of carbon-based materials. The mechanical stability and

biocompatibility of CNTs was questioned by certain researchers [93], glassy carbon is very brittle and might compromise the mechanical stability of the electrodes [94] and nanoporous boron-doped diamond has heavy fabrication constraints that difficult its embedding in flexible devices [92].

Thus, there is yet no ideal electrode material for bidirectional neural interfacing at the micrometre-scale.

1.3 Engineered Graphene for Neural Interface

1.4 Scope of this thesis

This thesis explores the development of neural implants technology based on EGNITE, a highly porous thin film electrode material made of graphene. This material has been designed to overcome the interfacing resolution and stability limitations of currently existing electrode materials used in implants to record and stimulate the neural activity.

Chapter 2 starts describing the synthesis of EGNITE and its physicochemical properties. Then, it discusses the development of wafer-scale fabrication process of thin and flexible neural probes for high resolution neural recording and stimulation. The development of the electrode material and the development of a stable fabrication process to produce devices with arrays of EGNITE microelectrodes are the main contributions of this work and the ones that took the longest time during the realisation of this thesis. To conclude, the chapter presents the electrochemical characterisation and stability study of the 25 μm diameter EGNITE microelectrodes, embedded in the fabricated implants. Microelectrodes based on this material exhibit low Z, extremely high CIL, and outstanding stability.

Chapter 3 explains the experiments performed in vitro and in vivo in rodents to assess the performance of the developed neural implants technology for bidirectional neural interfacing. Preliminary results of an in vitro biocompatibility study are first presented. Epicortical recording experiments performed with EGNITE exhibit low intrinsic noise and high SNR, reaching the limit of currently available electronic equipment. Neural stimulation via intraneural EGNITE implants is demonstrated to activate specific subsets of axons within the fascicles of the sciatic nerve with low current thresholds and high selectivity. Finally, visual percepts are proven to be

elicited in the visual cortex of rodents by EGNITE subretinal implants with smaller electrodes than the ones currently used by clinical devices.

To conclude, Chapter 4 summarises the contributions and findings of this thesis and explores the possibilities of the EGNITE technology to be used for clinical therapies.

2

EGNITE neural implants technology

A más cómo, menos porqué.

Jorge Wagensberg

This chapter presents Enigneered Graphene for Neural Interface (EGNITE), a thin film and highly porous graphene-based material developed to overcome the limitations of currently existing materials used in neural electrodes. Here, it is first described the synthesis of such material and its physicochemical properties. This chapter also describes the integration of EGNITE microelectrodes in dense arrays using flexible substrates. Finally, the electrochemical characterisation of the fabricated microelectrodes shows their high performance and remarkable stability.

2.1 EGNITE material

2.1.1 Material synthesis

2.1.2 Physical structure

2.1.3 Chemical composition

2.2 Neural implants fabrication

2.2.0.1 Wafer scale fabrication of neural implants based on EGNITE

2.2.1 Further fabrication developments

2.3 Electrochemical characterisation of EGNITE microelectrodes

3

Neural implants applications

Que tot està per fer i tot és possible.

Miquel Martí i Pol

This chapter presents preliminary in vitro biocompatibility results of EGNITE and explores the use of neural implants based on this material in the three potential applications: brain monitoring, peripheral nerves stimulation and the retinal implants. Neural implants interfacing the brain, nerves and retina are currently used in clinics to treat a wide variety of pathologies. However, the used devices suffer from functional and safety limitations, partly because the standard metallic electrodes loose their functionality when miniaturised to cellular level. EGNITE, however, exhibits optimal properties to interface with the neural tissue at such level. To assess the functional bidirectional interface of EGNITE in the three tissues of interest, we adapted arrays containing 25 μm diameter microelectrodes to specific designs for the brain, the nerves and the retina and carried out proof of concept experiments. The data of the neural recording study, is comparable to the state-of-the-art recordings with such small electrodes. In the neural stimulation study, we stimulated specific fibers inside the sciatic nerve and the retina with electrodes of 25 μm diameter, setting a new state-of-the-art.

3.1 In vitro biocompatibility: preliminary data

EGNITE thin films are intended to be part of an implanted device and directly interface with cells, therefore their biocompatibility is of vital importance. When used as substrates for cell growth, graphene-based materials have shown biocompatibility with various tissues [95, 96]. Here we present preliminary results of an in vitro biocompatibility study of EGNITE that has been conducted in collaboration with the NanomedicineLab from the University of Manchester.

To assess the biocompatibility of our EGNITE films, we first tested the adsorption of serum proteins, used here as a strong predictor of cell ability to attach and proliferate on those substrates. EGNITE films were compared to normal tissue-culture polystyrene (TCPS) and PEDOT:PSS (PEDOT), a conductive polymer that has attracted a lot of attention for neuronal interface applications. This was assessed through a bicinchoninic acid (BCA) assay (Figure 3.1a), which showed no significant difference between EGNITE and TCPS. The mass of adsorbed protein on PEDOT was slightly higher, likely due to higher surface roughness.

We then went on assessing the viability of human neuron-like cells (SHSY5Y cell line) after 24 hrs or 48 hrs of growth on the different substrates, using the resazurin reduction assay and measuring the relative alamar fluorescence (Figure 3.1b) [97]. TCPS with 10% DimethylSulfoxide (DMSO) added to the media was used as a positive control for cell death. Surprisingly, the viability of SHSY5Y cells doubled relative to the TCPS, after 48 hrs culture on EGNITE films. A significant but less dramatic increase of viability was also seen for cells grown on the PEDOT substrates. When using a modified lactate dehydrogenase (LDH) assay, measuring the amount of LDH present in viable cells by looking at the relative adsorbance , similar results to the resazurin reduction assay were obtained (Figure 3.1c). To decipher whether the observed increase in viability was due to increased cell metabolic activity or increase in cell number (i.e. cell proliferation), we performed cell counting after 48 hours (Figure 3.1d). Cell count from EGNITE films suggested that the increase in resazurin fluorescence was caused by an increase in cell proliferation rather than an increase in their metabolic rate, with a doubling amount of cells on EGNITE compared to TCPS. In contrast, for PEDOT substrates, the increase in viability using the resazurin assay appeared to be associated more to an increase in metabolic activity than cell number, as no significant difference could be revealed when comparing PEDOT and TCPS. Immunofluorescence microscopy of SHSY5Y cells stained with anti-β-III tubulin antibodies and counterstained with DAPI revealed that cells were

more spread, healthy and numerous on EGNITE compared to PEDOT or TCPS (Figure 3.1e-g).

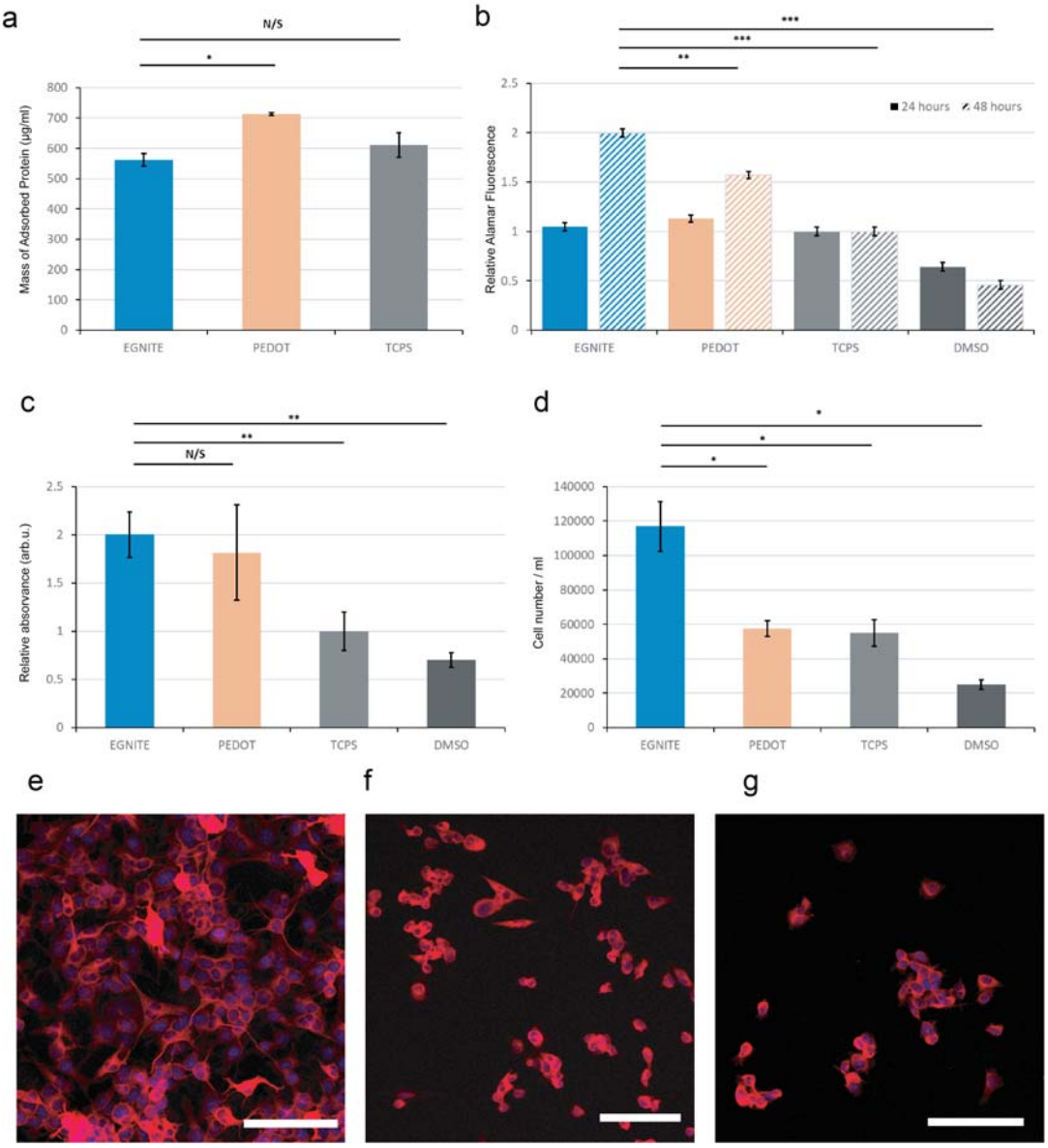

Figure 3.1: a. BCA assay to assess protein adhesion on substrates (n=4). **b.** Resazurin reduction assay performed on SHSY5Y cells grown on substrates for 24 or 48 hrs to assess viability (n=8). **c.** Modified LDH assay performed on SHSY5Y cells growing on substrates for 24 h to assess cell death by loss of membrane integrity. **d.** Trypan blue assay performed on SHSY5Y cells grown on substrates for 48 hours to assess cell count (n=4). Fluorescence micrograph of SHSY5Y cells stained for β-III tubulin (red) and DAPI (blue) and grown for 48 hrs on EGNITE **e.** , PEDOT:PSS **f.**, or TCPS **g.**. * = p< 0.05; ** = p< 0.001; *** = p< 0.0001. All scale bars are 100 μm.

Lastly, we interrogated the long term viability of primary neurons extracted from neonatal rat hippocampus on EGNITE. After 14 days of culture, neurons grown on EGNITE formed a network of well-individualised and branched neurons (Figure 3.2a), while neurons grown on glass coverslips tended to agglomerate and their extensions bundled (Figure 3.2b).

Overall, the preliminary data presented here indicate that EGNITE appeared biocompatible with cells that will be encountered in a neural tissue environment.

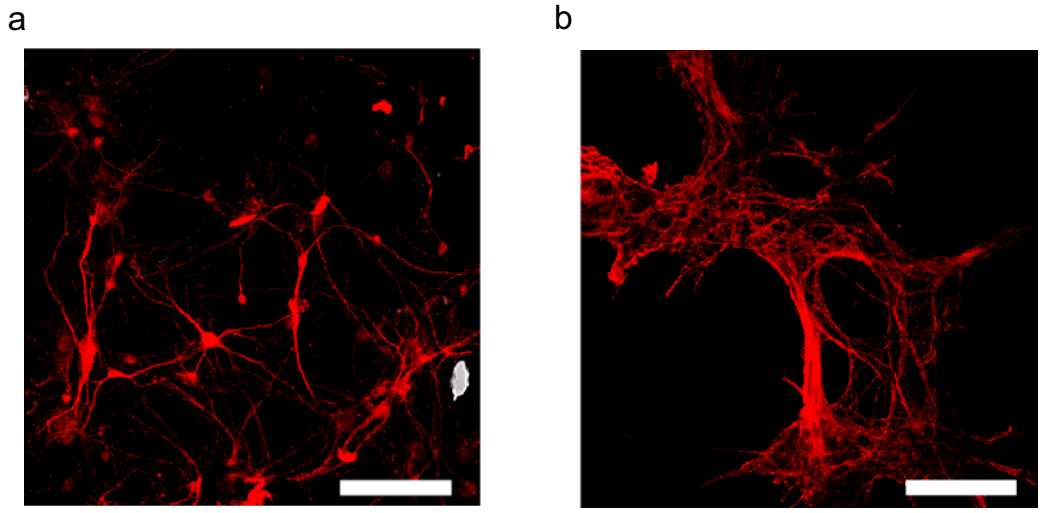

Figure 3.2: Fluorescence micrographs of primary hippocampal neurons stained for β-III tubulin (red) and grown for 14 days on **a.** EGNITE and **b.** glass, both coated with poly-L-Lysine. Scale bars are 100 μm.

3.2 Brain applications

Brain neural implants are devices that electrically record or stimulate the brain function in certain regions to diagnose and treat neural pathologies. Such devices usually consist of arrays of microelectrodes implanted inside the skull and connected to external electronic equipment responsible for the processing of the incoming or outcoming signals [18]. In the scope of this project, we focused on epicortical brain monitoring devices, i.e. implantable electrodes that are surgically placed on the surface of the dura or cortex in order to record signals from individual cells or groups of cells [98].

Current epicortical electrodes consist of flat-shaped interfaces made of Pt that are usually integrated in flexible devices with millimetre precision. With such technology, electrocorticography (ECoG) are carried out in clinics to identify and monitor pathologic and functional regions of the brain [98]. Examples of clinical uses are the localisation of the seizure focus to be resected in epileptic patients or the identification of functional and sensory regions during brain surgeries [99–104]. These devices can also be employed for brain-computer interfaces. One of the most notorious recent experiments in this directions has been the decipheration of intended speech using an epicortical array with 256 Pt electrodes [29].

The signal detection capabilities of technology based on Pt electrodes, have been surpassed by more advanced electrodes materials, such as PEDOT:PSS. The lower interfacial impedance of this material has permitted to miniaturise the microelectrodes to cellular dimensions and integrate them in micro-electrocorticography ($\mu ECoG$) arrays with resolutions in the range of tens of micrometres [30]. Following this same direction, in this section we present the neural recording capabilities of EGNITE $\mu ECoG$ arrays. The experiments described next were performed in collaboration with the BrainTech Laboratory (Inserm and Université Grenoble Alpes).

3.2.1 EGNITE technology for brain monitoring

The suitability of the graphene technology developed here to record in vivo neural signals was assessed by using flexible $\mu ECoG$ EGNITE devices to monitor the neural activity at the surface of the auditory cortex of anesthetised Sprague Dawley rats (Figure 3.3a). The $\mu ECoG$ devices consisted of arrays of 64 EGNITE microelectrodes ($\varnothing$ 25 μm) separated by 300 μm (Figure 3.3b). The microelectrodes exhibited an average impedance of 58 $\pm$ 25 kΩ at 1 kHz (Figure 3.3c). Following Equation 1.8, and assuming that the value is purely resistive, a rms noise of 1.5 μV could be expected.

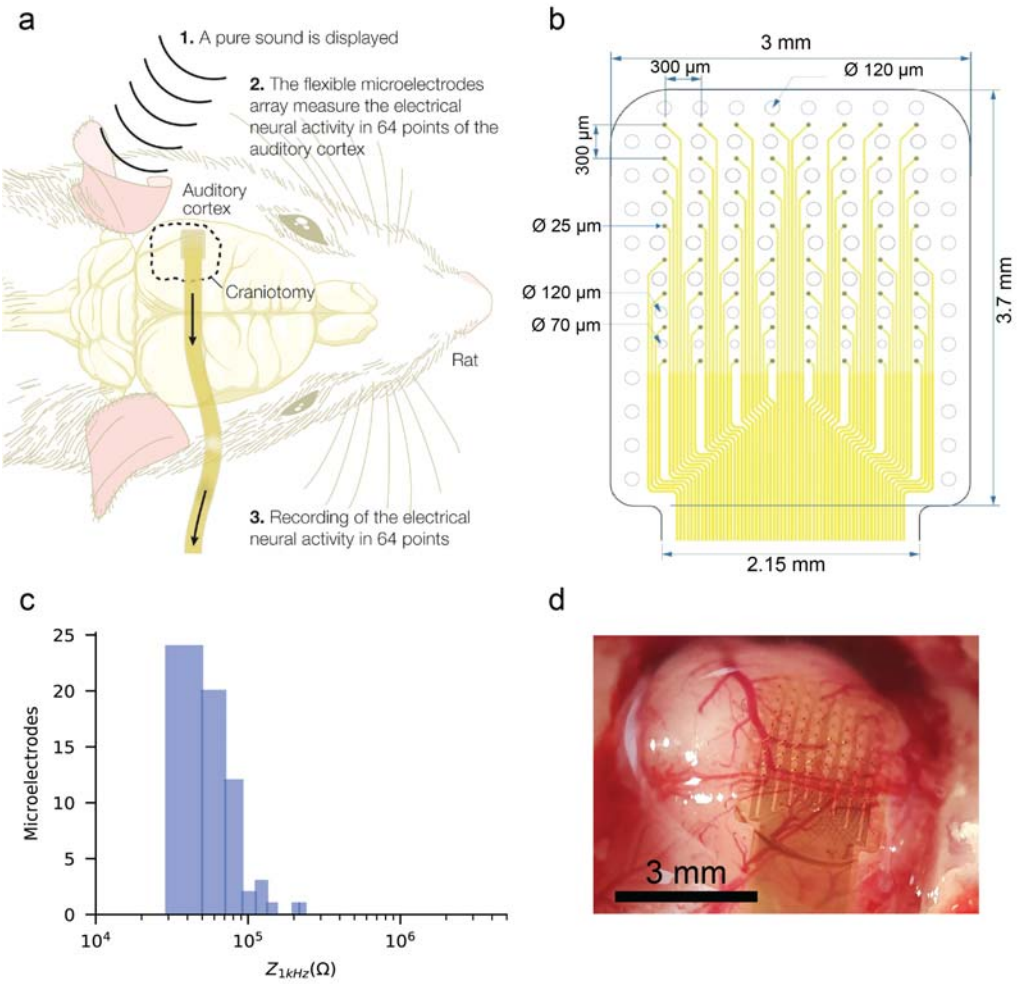

Figure 3.3: Epicortical neural recording setup. **a.** Schematic diagram of an acute experiment using an EGNITE $\mu ECoG$ flexible array to record epicortical neural activity of a rat. Evoked activity was induced by a pure 2 kHz - 16 kHz tone stimuli. **b.** Schematics of the flexible micro electrocorticographic array based on EGNITE microelectrodes used in this work. The array consists of a grid of 8x8 microelectrodes, spaced 300 μm from each other and they have a diameter of 25 μm. **c.** Impedances at 1 kHz before implantation of EGNITE $\mu ECoG$ devices, with 64 microelectrodes (average Z = 58 $\pm$ 25 $k\Omega$). **d.** EGNITE $\mu ECoG$ array on the auditory cortex of a rat.

The probe was positioned over the left auditory cortex (AI and AAF regions) (Figure 3.3d) and pure tones of frequencies between 2 kHz and 16 kHz and a duration of 200 ms (3 ms rise and 20 ms fall times) were presented at 90 dB sound pressure level (SPL) to generate evoked activity.

Figure 3.4 shows the 10 Hz high-pass filtered signal from each of the 64 EGNITE electrodes in the array recorded over 350 ms (where at t = 30 ms the 200 ms, 16 kHz tone was presented). The mapping corresponds to a single event in which large and sudden negative and positive peaks of the recorded signal after the onset and

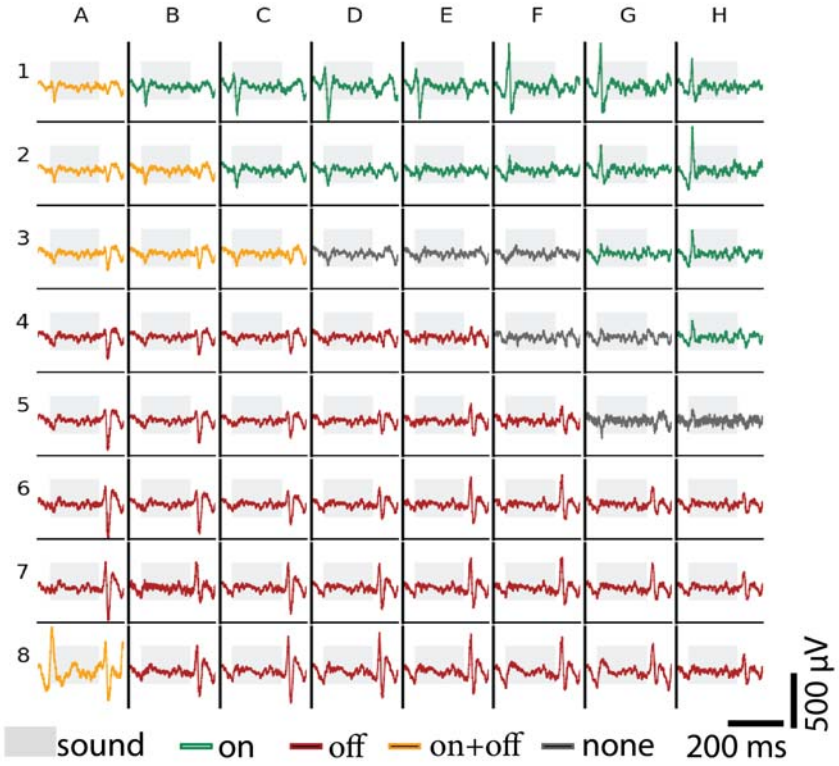

Figure 3.4: Mapping of the evoked neural activity depicting a single event across all 64 EGNITE microelectrodes. Depending on the region, onset (green), offset (red), both (yellow), or no onset/offset (dark grey) responses are recorded.

offset of the sound can be easily identified and indicate the existence of evoked local field potentials (eLFP) [105]. The high quality of the recorded signal allows to map single-events of eLFPs as the one displayed in Figure 3.4, which reveals a spatial clustering with ON responses (green) located on the top right corner and OFF responses (red) grouped in the bottom region. This is in agreement with previous reports, in which activation of cortical tissue upon the start or the end of an auditory stimulus has been observed in mammals [106, 107].

To further study the brain functional response to different stimuli, Figure 3.5a shows shows details of the ON signals recorded on signal trials, extracted from the region G1 of the device (as indicated in Figure 3.4) when pure tones of 2 kHz - 16 kHz were presented. Typically, the eLFP peaks are observed 20-40 ms after the onset of the sound signals, in good agreement with previous reports [105]. Representing the eLFPs maximum versus the frequency of the pure tones, a sigmoid-like shape could be fitted to the data (Figure 3.5b). No response, or very little response of less than 100 mV was observed for tones of 2 kHz and 4 kHz. However, for tones above the 8

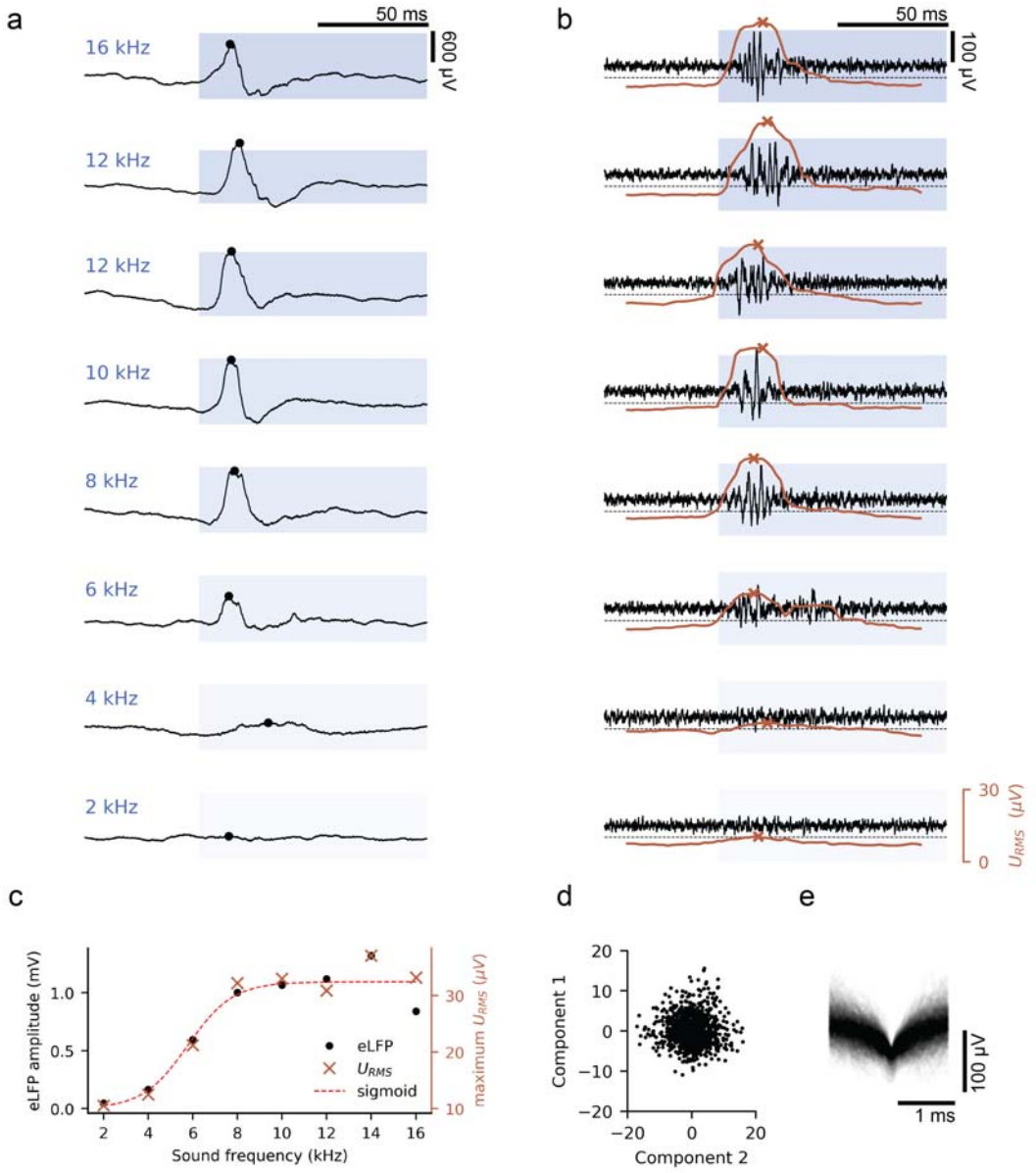

Figure 3.5: Analysis of eLFP when stimulating with different sound signals. **a.** Response of regions G1 to sound stimuli in terms of the evoked local field potentials (eLFP). **b.** These signals are high-pass filtered at 200 Hz to reveal high frequency MUA activity, confirmed by a simultaneous increase of the RMS value of the signal (brown). **c.** Maximum amplitude of the eLFP and the high frequency (>200 Hz) RMS signal versus the frequency of the stimulating tone. Both follow a sigmoid-like shape, indicating that the recorded neural tissue responds to frequencies above the threshold of 6 kHz. **d.** Principal component analysis (PCA) diagram, showing the first 2 fitted components. Only one cluster is identified. **e.** Wavelets identified by the algorithm around peaks of less than -30 μV.

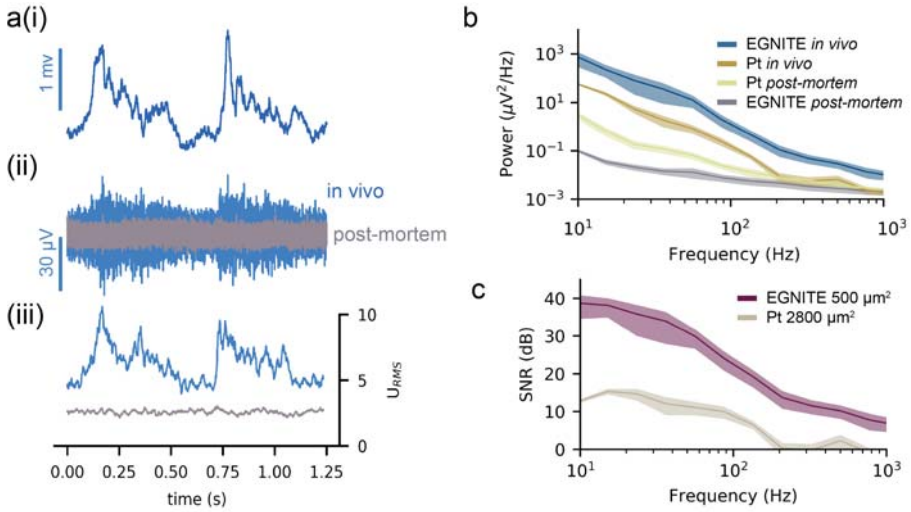

Figure 3.6: Neural data noise analysis and benchmark. **a(i).** Raw signal of spontaneous activity recorded with EGNITE microelectrodes. **a(ii).** The signal from a(i), filtered at 200 Hz. **a(iii).** Corresponding RMS value of the signal from a(ii). The grey line in a(ii) and a(iii) corresponds to the intrinsic noise of the microelectrodes. **b.** Averaged PSD of 60 microelectrodes of EGNITE ($\varnothing 25 \mu m$) and 60 of Pt ($\varnothing 60 \mu m$) in in vivo (blue and brown, respectively) and post-mortem (grey and yellow, respectively) conditions. **c.** Averaged SNR of 60 microelectrodes of EGNITE and 60 of Pt, calculated from the ratio of the in vivo and the post-mortem signals shown in b.

kHz, the eLFPs consistently reached values of about 1-1.2 mV. The 50 % amplitude was reached at 6 kHz.

Figure 3.5b shows the same signals from the G1 region high-pass filtered at 200 Hz, overlapped with its root mean square (RMS) value. The high frequency multi-unit activity (MUA) and the corresponding increase of the RMS amplitude due to MUA nicely correlate to the eLFP from Figure 3.5a, indicating a synchronous behaviour of the neurons to the stimulus [105]. The maximum RMS potential reached during the evoked response is plotted in Figure 3.5b as a function of the frequency. The response follows a sigmoid-like shape like the one observed for the eLFPs. We attribute this sigmoid-like behavior to synchronous response in the G1 region of neurons responsible for processing auditory stimuli of freqeuncies above 6 kHz. Individually, neurons exhibit this kind of behavior, consistently firing when receive a signal above their activation threshold. When synchronised, they elicit a much larger response in the shape of an eLFP [108]. To investigate in more detail the high frequency MUA and to try to identify contributions from single neurons, a spike sorting algorithm was run on the data. That software first identified peaks below -30 μV and extracted wavelets of 1 ms before and after these points. Then, it analysed the wavelets using a principal component analysis (PCA) using 5 components and attempted an automatic

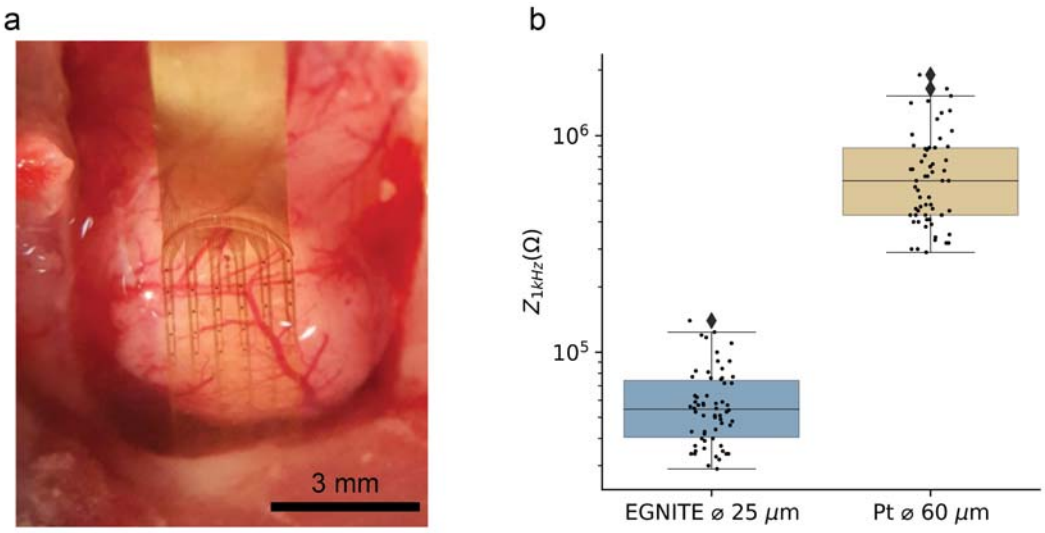

Figure 3.7: *μECoG* device with Pt-based electrodes. **a.** Flexible array of 60 Pt microelectrodes of 60 μm diameter (E64-500-20, NeuroNexus, USA) placed on the auditory cortex of a rat. **b.** Impedance comparison between an EGNITE array of 64 microelectrodes of 25 μm diameter and a Pt array of 60 microelectrodes of 60 μm diameter.

clustering using such fitted components. Only one cluster was identified, as Figure 3.5d shows; therefore, no single neuron activity was identified. Figure 3.5e shows, overlapped, the extracted wavelets. Such wavelets consists of negative peaks but present no reproducibility. The spike sorting algorithm was custom developed on Python 3 using the Neo, Elephant and Sklearn libraries [109].

The recording capabilities of EGNITE microelectrodes are further confirmed by evaluating spontaneous activity recordings (Figure 3.6a(i)). The high-pass filtering of the signal at 200 Hz shown in Figure 3.6a(ii) uncovers the contribution of low-amplitude (20-30 μV peak-peak) high frequencies, which disappear post-mortem as assessed by the grey curve. Similarly to the evoked activity signal shown in Figure 3.6, the calculation of the RMS value of the signals allows correlating the low frequency activity (<50 Hz) of the spontaneous activity with high frequency activity (>200 Hz). The intrinsic RMS noise of the electrode (calculated from the post-mortem recordings) was of 2.5 μV, which is very close to the technical capabilities of the electronic setup [30, 110]. Figure 3.6b shows the averaged power spectral density (PSD) obtained from 60 EGNITE electrodes over a 30 minute in vivo recording, compared to the PSD of a post-mortem recording. The SNR (calculated from the division of both signals) reaches 40 dB at 10 Hz and 5 dB at 1 kHz (Figure 3.6c), demonstrating an excellent capability to record high fidelity signals at both low and high frequencies [111].

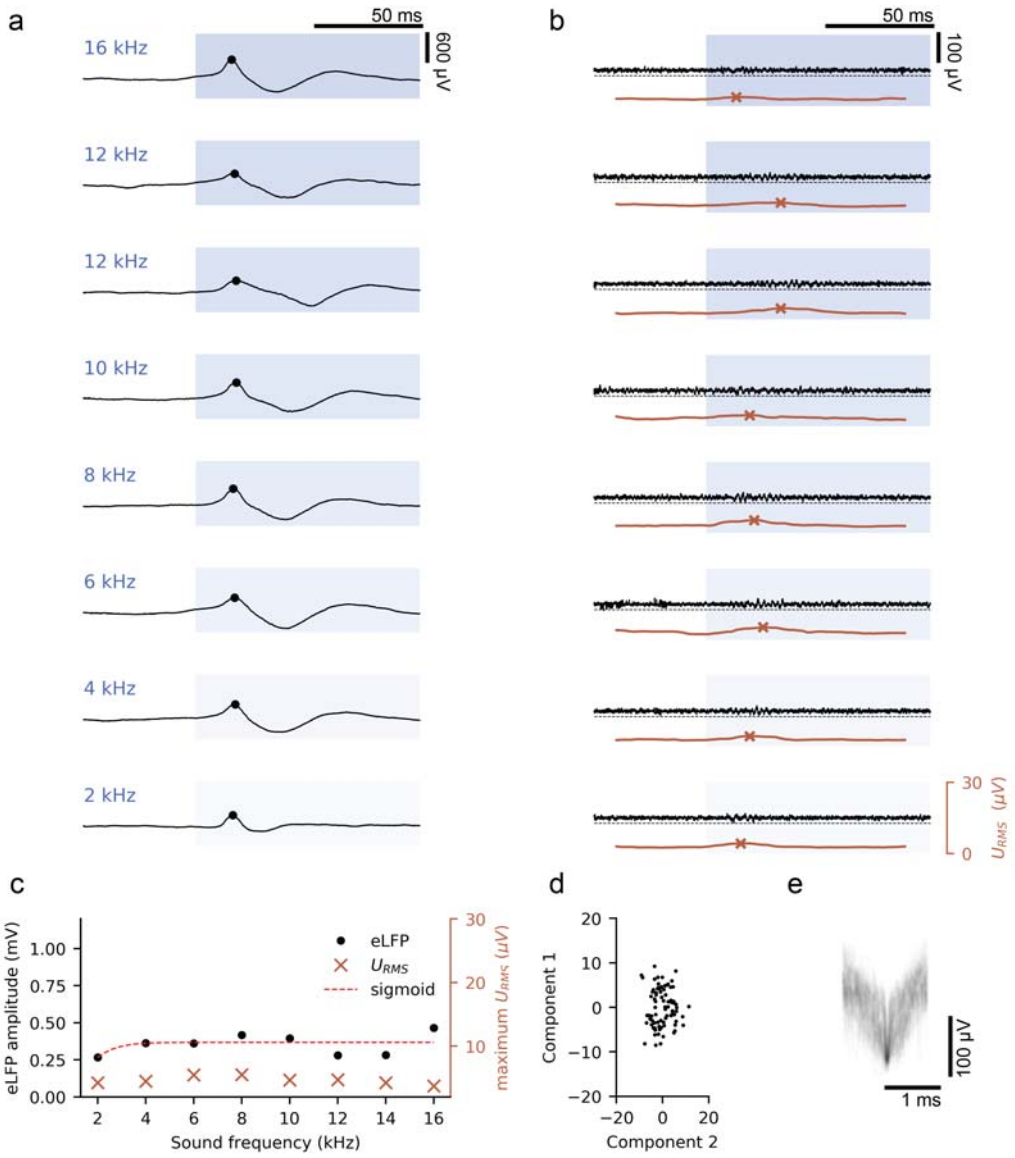

Figure 3.8: Analysis of neural recording data of Pt electrodes ($\varnothing$ 60 μm). **a.** Response of a single Pt electrode to different auditory stimuli. A similar eLFP is obtained for all the stimuli. **b.** These signals are high-pass filtered at 200 Hz to reveal high frequency MUA activity. However, no activity above the baseline was detected. The brown line corresponds to the RMS value calculated over moving windows of 20 ms. **c.** Maximum amplitude of the eLFP and the high frequency RMS versus the frequency of the stimulating tone. **d.** Principal component analysis (PCA) diagram, showing the first 2 fitted components. Only one cluster is identified. **e.** Wavelets identified by the algorithm around peaks of less than -15 μV.

To benchmark the recording capabilities, similar measurements were performed on the same animal using a CAE of Pt of 60 μm of diameter (E64-500-20, NeuroNexus) (Figure 3.7a). The average electrode impedance was 695 $\pm$ 361 $k\Omega$, which is one order of magnitude larger than the 25 μm diameter EGNITE microelectrodes (Figure 3.7b). In average, evoked and spontaneous signals of lower amplitude were recorded with 60 Pt electrodes while the noise recorded in the post-mortem conditions was higher than the one recorded by EGNITE microelectrodes (Figure 3.6b). The obtained SNR was 15 dB at 10 Hz and dropped to 0 dB in average for frequencies higher than 200 Hz, indicating that the high frequency MUA could not be registered with Pt electrodes (Figure 3.6c). The analysis of evoked activity shown in Figure 3.8 confirms such limitation. In this case, the electrode was located on top of a region that responded at all the tones with eLFPs, but no high frequency MUA was detected. The origin of such limitation is the high impedance and large area of the Pt electrodes. Overall, EGNITE technology overcomes the limitations of Pt electrodes by being able to record with higher fidelity highly spatially localised signals.

3.3 Peripheral nerve applications

The extension of the nerves all across our bodies and their indispensable role in signal transmission make them a very interesting target for electrical interfacing. From them emanate crucial body functions such as the movement, sensations and hormones control [4].

To monitor or modulate such functions for medical purposes, bidirectional neural interfacing with the nerves has been long investigated [26, 112–114]. However the information in the nerves is extremely difficult to access. Nerves consists of bundles of densely packed axons, whose cross sections can reach up to 15.000 fibers/mm^2 [4]. Then, each fiber covers less than 70 μm^2 of the cross section in average. To optimally modulate them, the ideal neural interface should resolve signals and provide stimulation within this spatial resolution [26]. One of the most relevant advances in the field has been the development of intraneural electrodes to bidirectionally interact with robotic limbs for patients who went through an amputation [114]. Those electrodes, implanted in distal nerves close to the patient amputation, can record intended movement and provide sensory feedback from the artificial limbs. Current technology is able to stimulate with microelectrodes of 80 μm diameter [115]. Further miniaturisation of the electrodes would permit to access to a richer variety of movements and sensations [26, 114].

In this section we evaluate the capabilities of EGNITE to electrically stimulate specific neural fibers within nerves using microelectrodes of 25 μm diameter. The experiments described next were carried out in collaboration with the Group of Neuroplasticity and Regeneration from the Institute of Neurosciences of the Universitat Autònoma de Barcelona.

3.3.1 EGNITE technology for nerve fibers stimulation

EGNITE MEAs were adapted to a transverse intrafascicular multichannel electrode (TIME) design, which has been used in previous work to stimulate the sciatic nerve of rats and humans [114–117]. In our design, however, we increased the density of active sites with respect to the last report from 2.5/mm to 7.4/mm [115]. The device consisted of 2 linear arrays (A and B) of 9 electrodes ($\varnothing$ 25 μm) along a 1.2 mm stripe. Each linear array faced opposite sides of the stripe (Figure 3.9b). The devices were implanted transversally in the sciatic nerve of an anesthetised Sprague Dawley rat for acute experiments (Figure 3.9a). Once implanted (Figure 3.9c), the device crossed the peroneal fascicle (responsible for the innervation of the tibialis

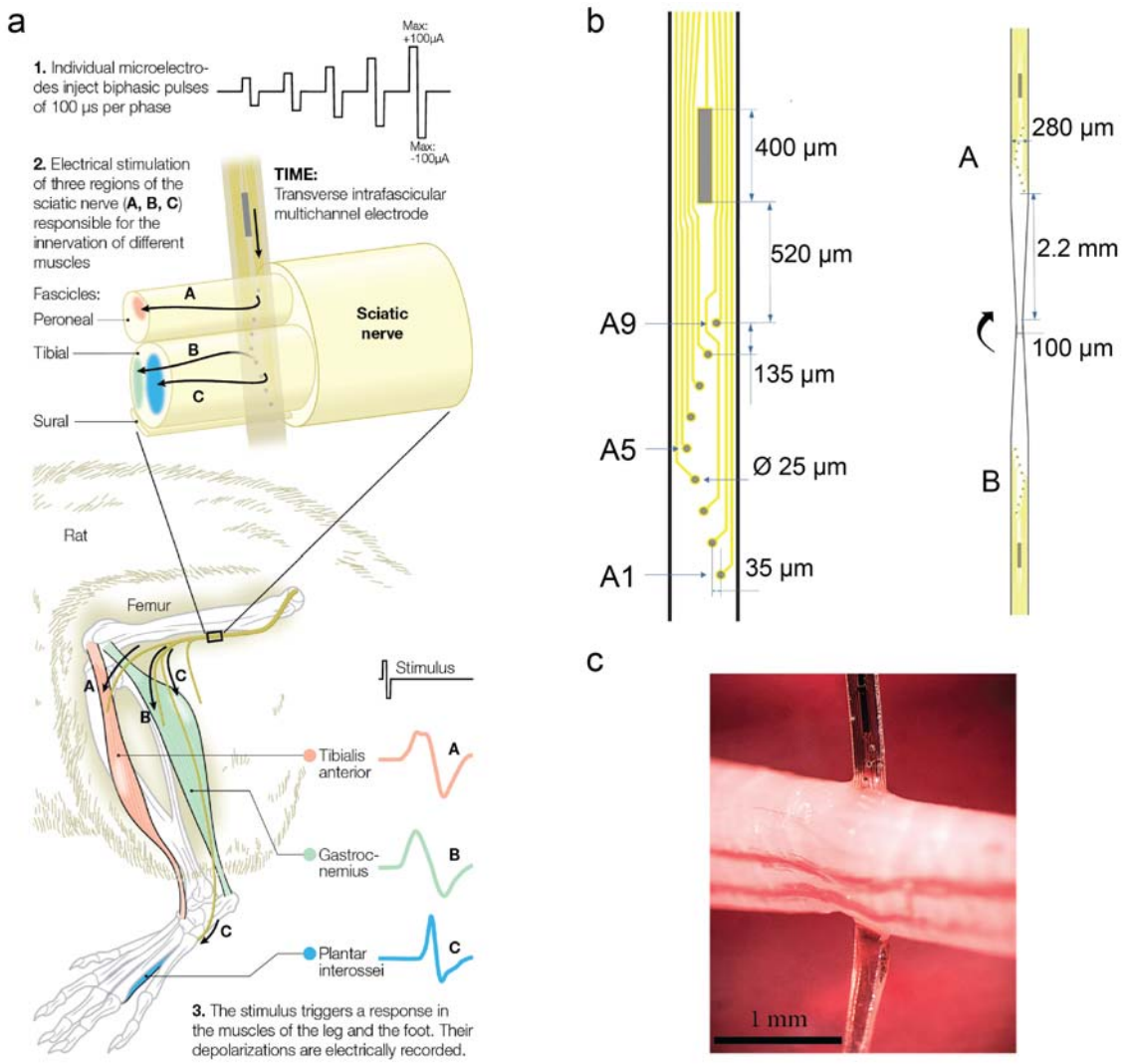

Figure 3.9: Sciatic nerve intrafascicular stimulation setup. **a.** Schematic diagram of the acute stimulation experiment. A transversal intra-fascicular microelectrode array (TIME) is implanted in the sciatic nerve of a rat crossing the peroneal and the tibial fascicles. The innervation of TA muscle can be found in the peroneal fascicle, whereas the GM and PL muscles innervation is located in the tibial fascicle. Biphasic pulses of 100 $\mu s/phase$ and a maximum amplitude of 100 μA were injected individually at the 9 microelectrodes of 25 μm diameter located in the device. The local electrical stimulation can depolarise the nerve fibers from its vicinity and trigger the electrical activity of the muscles, which was recorded with needle electrodes. **b.** Schematics of the Transverse Intrafascicular Multielectrode (TIME) probe based on EGNITE used in this work. Once the device is folded for implantation, two linear arrays with 9 microelectrodes of 25 μm diameter and a large rectangular electrode face opposite sides of the stripe. In this work, only data from side A is considered. **c.** Optical micrograph of the implanted TIME device in the sciatic nerve.

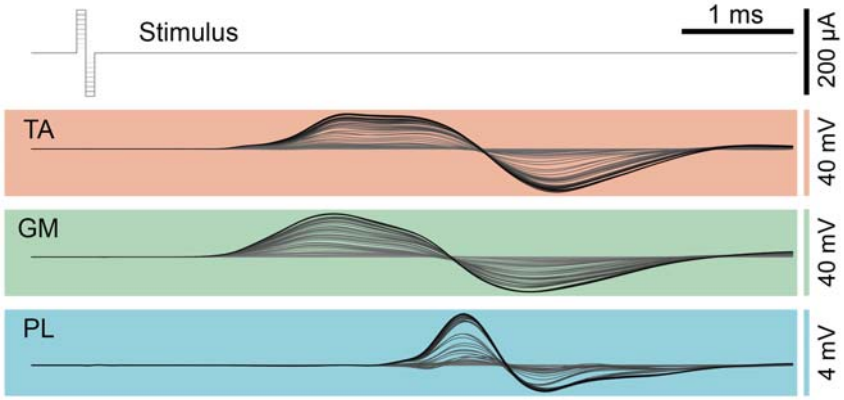

Figure 3.10: Compound muscle action potentials (CMAPs) recorded from the TA, GM, and PL muscles in response to increasing levels of injected current pulses applied to one of the electrodes.

anterior (TA) muscle) and the tibial fascicle (responsible for the innervation of both the gastrocnemius (GM) and plantar interosseous (PL) muscles). Each electrode in the EGNITE array was individually stimulated and the elicited compound muscle action potentials (CMAP) of the TA, GM, and PL muscles were simultaneously recorded by monopolar needles inserted on the muscles bellies [116] (Figure 3.10). As a reference electrode it was used the large rectangular electrode located on the same TIME device. Details of the protocol followed are explained in the section 5.3 of the Appendix.

To stimulate the nerve, trains of 100 biphasic pulses (100 $\mu s/phase$) with increasing current amplitude at 3 Hz, ranging from 0 to 100 μA (using 2 $mC/cm^2/phase$), with steps of 1 μA, were injected through each of the microelectrodes.

Figure 3.11a shows the recorded response of TA, GM and PL muscles to these current pulses applied to the A1-A9 microelectrodes. The recorded signals are normalised to the maximum amplitude of the CMAP. The first recorded CMAP appears at very low intensity of stimulation, with a threshold current of about 15-20 μA and then shows a fast increase in amplitude until the maximum activation is reached. The recruitment curves reflect the typical sigmoidal shape. This is the curve towards which tends the amplitude of the response of a healthy motor unit action potential (MUAP) under a linear increase of the current [118–120] (Figure 3.11b). Parameters of the sigmoid curve, such as the activation threshold or stepness of the CMAP scan depend on the current stimulating the MUAP innervation [118]. Thus, the pattern of muscular activation changed depending on the stimulating electrode and the signals applied. The activity could be split in 2 clusters: one for A1-A5, in which the TA muscle was activated at lower stimulus intensity than the GM and the

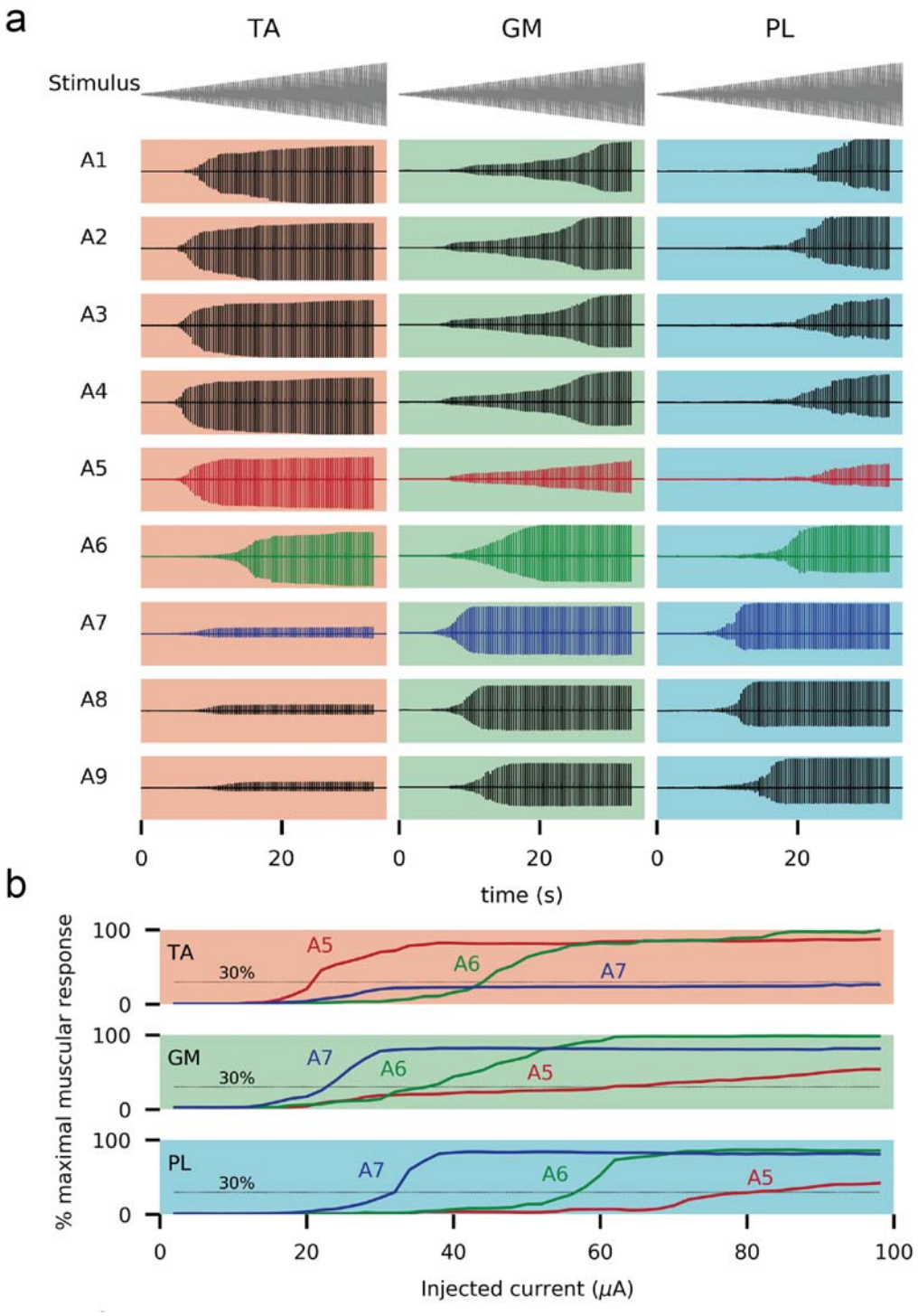

Figure 3.11: Compound muscle action potentials (CMAPs) of multiple electrodes stimulation. **a.** Recorded CMAP in TA, GM, and PL muscles in response to trains of biphasic current pulses of increasing amplitude applied to the 9 microelectrodes of the array A, at one side of the TIME. **b.** Normalised CMAP of TA, GM, and PL muscles in response to pulses injected to microelectrodes A5-A7 from the implanted TIME.

PL muscles, and another one for A7-A9, in which the GM and PL muscles exhibited more activity than the TA muscle. This suggests that the first five microelectrodes were placed in the peroneal fascicle, whereas the last three were located within the tibial fascicle. From these responses, critical parameters for implants aiming at restoring mobility such as current thresholds and selectivity index of the modulated the muscular activity can be derived [26, 114, 116].

Of particular interest are electrodes A5-A7, which are located nearest the interface between the two peroneal and tibial fascicles. In these electrodes, significant changes of current threshold and selectivity index were observed. Using 30 % of muscle activation as a benchmark, which is the minimum stipulated to overcome gravity, the current stimulation at which this occurred for each muscle was determined [116]. The pulse current needed for evoking a CMAP of 30 % the maximal amplitude in the TA muscle was 21 μA when stimulated by A5, 45 μA by A6, and could not be achieved by A7 (Figure 4e). For the PL muscle the current was 33 μA when activated by A7, 45 μA by A6 and 81 μA by A5. Similarly, GM muscle required 23 μA when activated by A7, 37 μA by A6 and 62 μA by A5. From these data, a selectivity index above 0.85 was calculated for the 30 % activation of the TA, 0.77 for the GM, while for the PL it was only 0.44. As an indicator, an optimal selectivity index of 1 indicates that one muscle can be solely activated without any activation in the other recorded muscles [26, 114]. Taking into account that the TA innervation is conveyed through the peroneal fascicle and the innervations of the GM and the PL are contained in the tibial fascicle [121], the lower activation thresholds and higher selectivity indices are obtained for stimuli coming through electrodes placed in closer positions [115, 116]. Therefore, we can derive that A5 is located within the peroneal fascicle, A7 in the tibial fascicle, and A6 is likely between the two fascicles. The lower selectivity index obtained by the PL is probably due to the high dispersion of the nerve fibers innervating this muscle within the tibial fascicle compared to the more confined fibers of the TA and GM [121].

Figure 3.12a shows the minimum current thresholds to achieve a 5% and a 95% of the CMAP amplitude in TA, GM and PL muscles taking into account the activity triggered by all the microelectrodes shown in Figure 3.11a. To reach 5% contraction, less than 50 μA were required for all the muscles; similarly, less than 100 μA were needed to reach 95% of maximal activity. Compared to previous studies in which larger electrodes of iridium oxide were used (IrOx, $\varnothing$ 80 μm) [115], EGNITE electrodes elicited a response with thresholds 2 to 3 times lower.

The selectivity index values achieved with EGNITE electrodes slightly improved with respect to the ones previously obtained using larger IrOx electrodes for the TA and GM muscles, while it was lower for the PL muscle. Considering the higher dispersion of the PL innervation with respect to the ones of the TA and GM muscles and the smaller dimension of the stimulating EGNITE microelectrodes, we can derive a higher focality in the stimulation was achieved using EGNITE technology (Figure 3.12b) [26, 115, 121].

Thus, the high charge injection density of EGNITE allows the fabrication of smaller electrodes while keeping the stimulation functionality. As a result, the injected current is highly focalised into nearby regions, permitting a higher resolution and more efficient electrical stimulation of the highly confined TA and GM nerve fibers. Apart from the therapeutic advantage this can provide, the power consumed by the stimulation device can be significantly reduced and its functional lifetime could be eventually extended, even after fibrotic encapsulation [114, 115].

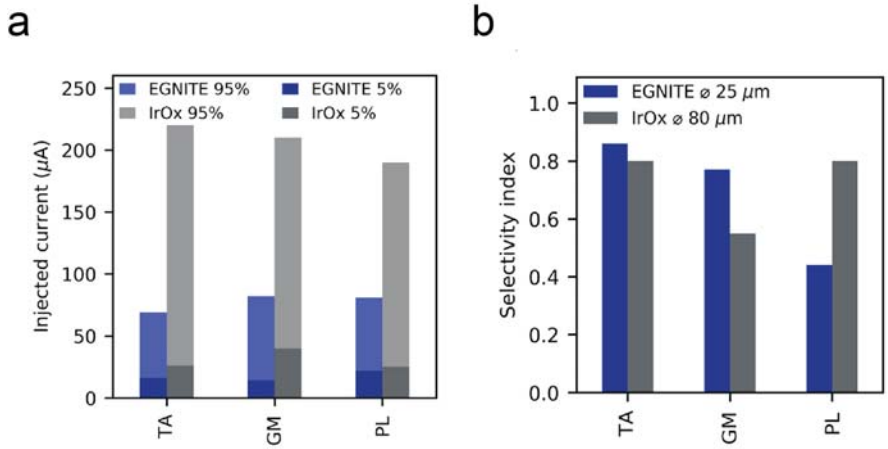

Figure 3.12: Benchmark of the stimulation EGNITE technology. **a.** Comparative plot of the injected current needed to elicit a 5 % and 95 % of the maximum CMAP using microelectrodes for EGNITE (blue) and IrOx (grey). **b.** Comparative plot of the selectivity index at the minimal functionally relevant muscular stimulation for EGNITE (blue) and IrOx (grey) [115].

3.4 Retinal applications

Vision restoration in blind patients using retinal implants has been intensively investigated over the last decades [122–125]. Many efforts have focused especially on restoring vision in patients suffering from retinis pigmentosa or age-related macular degeneration, diseases in which the photoreceptors degenerate.

The retina is the innermost light-sensitive layer of tissue of the eye, responsible for the transduction of light stimuli into neural signals to the optic nerve. It comprises three main layers with different functional cells: the photoreceptors, bipolar cells and retinal ganglion cells (RGCs). The photoreceptors are the first light transductors and send neural signals to bipolar cells. These ones perform a first processing of the signal and further transmit the information to the ganglion cells. These, in turn, add another processing layer and convey the information to the optic nerve. From there, the optic path continues to the brain, where the signal is processed in cascade in the Superior Colliculus (SC), Lateral Geniculate Nucleus (LGN) and the Visual Cortex (V1/V2) [4, 126–128]

Retinitis pigmentosa causes the light sensitive photoreceptors in the eye to degenerate, but a large proportion of the bipolar cells and retinal ganglion cells within the inner retina survive [129, 130]. These surviving neurons can be electrically stimulated by a spatiotemporal electric field pattern generated by an array of electrodes to produce a signal that is transmitted to the brain and can be interpreted as a visual percept [131]. Following this approach, two kind of retinal implants have been proposed: subretinal and epiretinal implants. The first approach aims at stimulating the activity of the bipolar cells, while the second directly targets the RGCs. Because of the bipolar cells preprocessing of the signal has proven to be important for the coherence of the signal once in the brain, the subretinal approach seems more convenient [131, 132]. To achieve functional vision restoration, the electrical pattern should mimic the original spatiotemporal characteristics previously generated by the photoreceptors [133–136]. For that, the stimulation resolution should draw near single cell resolution [137]. To trigger an action potentials in the retina under in vitro conditions, charges about 0.5 and 2 nC are known to be required for mammal retinas. In the chronic in vivo case, the required charge can be more than 10 times larger [138]. Additionally, the stimuli should be delivered with millisecond-scale precision to mimic the behavior of photoreceptors [137].

To evaluate vision restoration in humans, visual acuity (VA) determines how well patients can identify shapes [139]. A VA of 0.4 is required for normal reading without

visual aids, 0.3 is already considered 'low vision', 0.1 is necessary for self-sustained orientation and navigation, and values below 0.02 are considered blindness [139, 140]. Following the subretinal approach, retinal implants currently in commercialisation have been able to partially restore vision in patients with retinitis pigmentosa. For example, Argus II (Second Sight Medical Products) is a device with 60 microelectrodes of Pt, each of a diameter of 200 μm, that can restore vision up to an acuity of 0.015 [141]. The Prima device (Pixium Vision), with 378 microelectrodes spaced 100 μm could improve the results to 0.04, helping patients to identify large letters [142]. To further improve the outcome of retinal implants, higher stimulation resolution is required. For that, even smaller, higher performing and more stable electrodes are necessary [137]. EGNITE, with its CIL of more than 8 mC/cm^2 and high stability, could enable further electrode miniaturisation to increase the density of the interface and thus, mimic the action potentials pattern on a more naturalistic way.

In this work, we present a proof of concept of the EGNITE neural implant technology for vision restoration applications. For that, we first show the capabilities of an EGNITE array to electrically record and stimulate the neural activity of an explanted retina. Moving to in vivo applications, we observed the activation of the visual neural path in the brain of a rodent by functional ultrasound, when the retina was electrically stimulated with electrodes of 25 μm diameter from an EGNITE subretinal implant. These experiments were performed in collaboration with the Institute de la Vision from Paris.

3.4.1 EGNITE technology for in vitro bidirectional neural interface

For the in vitro assessment of the bidirectional interfacing capabilities of EGNITE microelectrodes with the retinal tissue, an explanted retina was mounted on a rigid EGNITE MEA to monitor its electrical activity when light and electrical stimuli were applied (Figure 3.13a).

The array contained electrodes of 25, 50 and 100 μm of diameter (Figure **??**f), which exhibited an impedance at 1 kHz of 35 $\pm$ 5 $k\Omega$, 11 $\pm$ 3 $k\Omega$ and 9 $\pm$ 2 $k\Omega$, respectively. The details of the retina preparation are explained in the Appendix, as well as the protocol followed to fabricate the rigid array on a transparent pyrex substrate. To monitor the electrical activity of the tissue, a Ag/AgCl pellet was introduced in the bath as a reference electrode. Figure 3.13b shows an optical micrograph of the retina placed on the EGNITE MEA, with the photoreceptors

facing against the electrodes in a subretinal configuration. During the experiments the preparation was kept in the dark and perfused with standard solution.

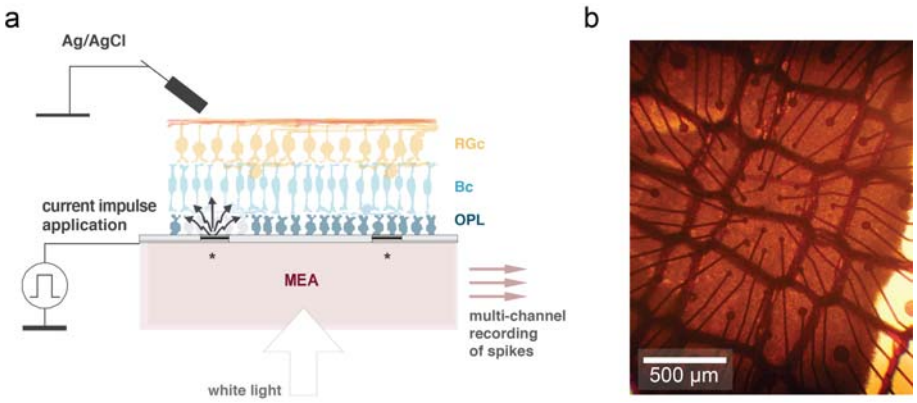

Figure 3.13: Setup for ex vivo stimulation experiments mimicking the subretinal implant situation. **a.** An explanted retina was attached to an array of planar microelectrodes with the photoreceptor side down for light and electrical stimulation. **b.** Optical micrograph of the explanted retina on the EGNITE MEA array.

Light stimulation. Full field light stimuli (λ = 445 nm) were projected to the tissue in trains of 20 pulses, each of 2 s duration, at 0.1 Hz through the MEA. Figure 3.14a presents a 200 Hz high-pass filter signal recorded by a 25 μm EGNITE electrode when the retina was illuminated (blue shadow). There, negative peaks of 1 ms duration and peak-to-peak amplitudes of more than 40 μV were identified as responses from different retinal ganglion cells (RGCs).

The neural data was processed with a custom developed spike sorting algorithm to identify contributions from specific cells. The software was developed on Python 3 and the Neo, Elephant and Sklearn libraries were used [109]. The algorithm first identified negative peaks below -35 μV and collected wavelets of 1.5 ms duration around those points. Next, all the wavelets were analysed with a principal component analysis (PCA) algorithm using 5 components [143]. Figure 3.14b shows the PCA projection of the first 2 components fitted to the wavelets. For the clustering, the distance in the hyper-parameters space of the fitted components was manually determined to obtain reasonable results. Then, the software automatically clustered the data in 3 groups: the purple, the orange and the blue ones. Figure 3.14c shows, overlapped, the wavelets of each cluster. The wavelets exhibit the typical shape of single action potentials, with depolarisation amplitudes of few tens of μV and durations shorter than 1 ms. In the purple and the orange groups the shape of the wavelets is highly reproducible and the curves significantly differ from one another. The third cluster is

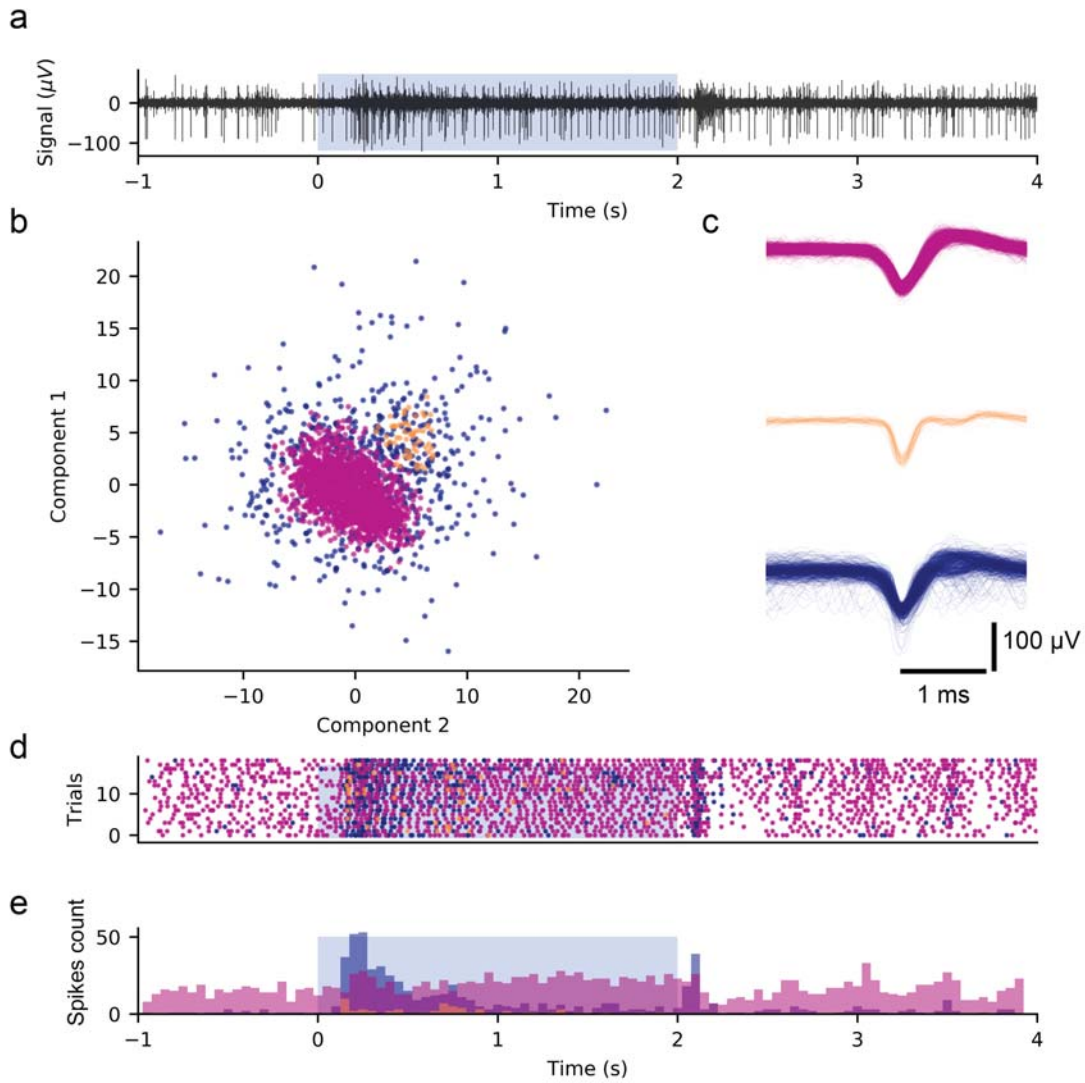

Figure 3.14: Data analysis of in vitro light stimulation recordings **a.** Electrical neural activity of the retinal tissue recorded with a 25 μm EGNITE electrode and high pass filtered at 200 Hz under light stimulation (blue shadow). **b.** 2-dimensional projection, using principal component analysis (PCA) and unsupervised clustering of neuronal activities. Two well defined clusters are identified (purple, orange) while a third one encompass less reproducible wavelets, probably coming from more distal neurons. **c.** Wavelets overlap, grouped by clusters. **d.** Raster plot with the activity of the different neurons. **e.** Peri-stimulus time histogram of the clustered neural activity.

considered by the algorithm not to have high enough reproducibility and classified as noise. Because of the higher reproducibility of the wavelets from the first 2 clusters, we can attribute them to spikes from individual RGCs [109, 143, 144]. We putatively associated the signals of the third group to spikes coming from different neighboring cells firing less systematically. To improve the spike sorting algorithm, we suggest to further develop the software and consider the clusters as a multivariate normal

distribution of single spikes, fit the PCA parameters and compute the probability of being mixed with another one [145].

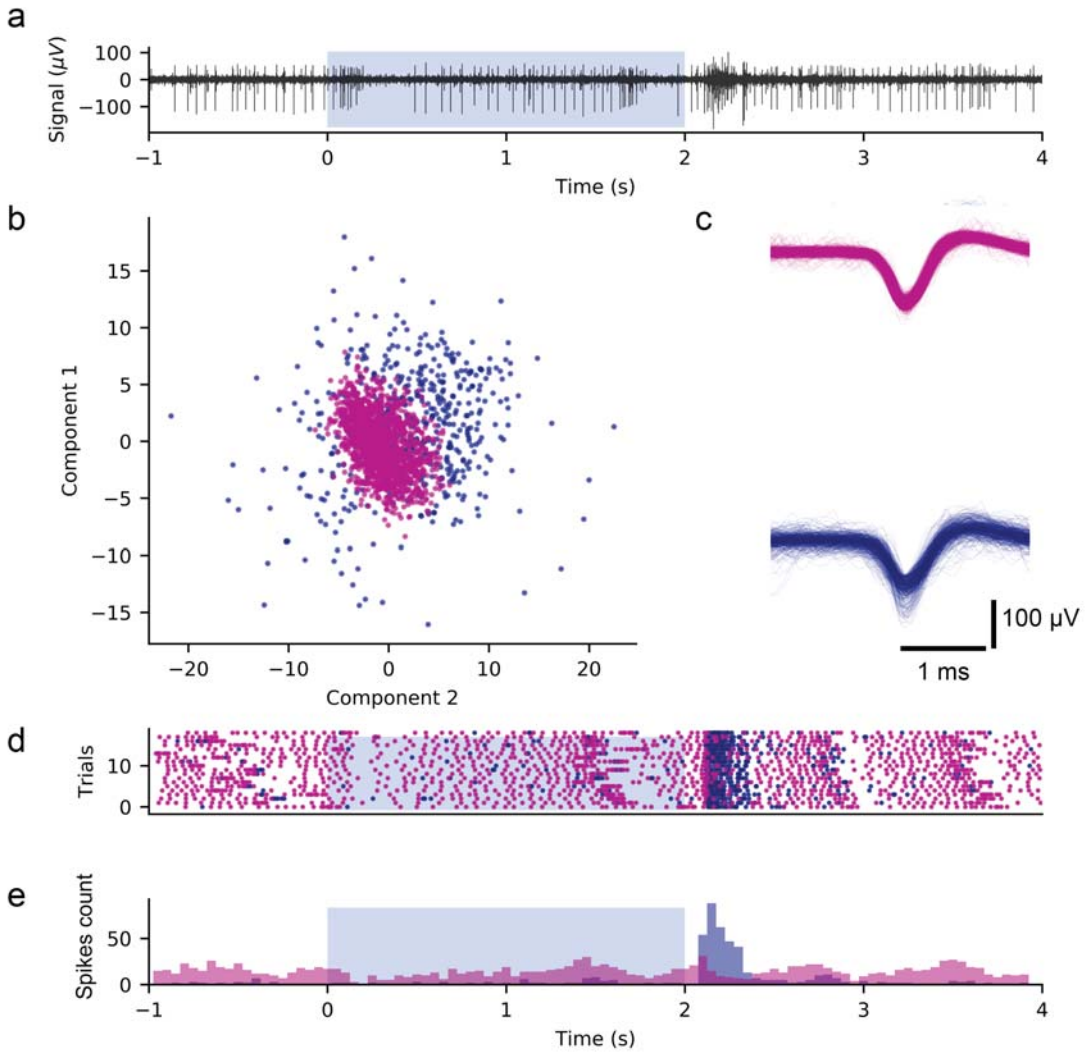

Figure 3.15: Data analysis of in vitro light stimulation recordings with L-AP4. **a.** Electrical neural activity of the retinal tissue recorded with a 25 μm EGNITE electrode and high pass filtered at 200 Hz under light stimulation (blue shadow) when L-AP4 was included in the perfusion solution to block the ON responses. **b.** 2-dimensional projection, using principal component analysis (PCA) and unsupervised clustering of neuronal activities. Only one well defined cluster is identified (purple) while the second one encompasses less reproducible wavelets, probably coming from more distal neurons. **c.** Wavelets overlap, grouped by clusters. **d.** Raster plot with the activity of the different neurons. **e.** Peri-stimulus time histogram of the clustered neural activity.

The raster plot from Figure 3.14d and the peri-stimulus time histogram (PSTH) from Figure 3.14e reveal that the behavior of the three clusters is significantly different. The spikes from the purple cluster are continuously fired, but their firing

rate decreases after the offset of the light stimulus. The orange wavelets are rapidly fired after the onset of the light. The contributions from the blue group can be identified both after the onset and the offset of the light stimulus. Comparing these behaviors with previous works, we classified the first neuron as ON-OFF direction-selective RGC and the second one as fast ON transient RGC, while the blue cluster contained contributions from fast ON and OFF step RGCs [146].

The spiking activity was further investigated by perfusing the retina with 50 μM L-AP4 (Tocris). This substance is an agonist for metabotropic glutamate receptors that mediate the ON signaling pathway in the retina and should block the response from fast RGCs [147]. Figure 3.15 shows the analysis we run on that data, similar to Figure 3.14. There, the PCA algorithm only clustered and identified the first neuron, the ON-OFF direction-selective RGC and still found a considerable contributions of less reproducible cells firing on the stimulus offset. However, no trace of the fast ON transient RGC was found, and also the contribution from less reproducible cells was absent after the stimulus onset, in agreement to the expected behavior. Thus, we confirmed the capabilities of EGNITE microelectrodes to successfully record single spikes activity under in vitro conditions.

Electrical stimulation. Next, we proceed to electrically stimulate the retina with a 25 μm diameter EGNITE electrode while the response of the nearby tissue was being monitored with adjacent electrodes (Figure 3.13a). For that, biphasic cathodic first current-controlled pulses of widths between 100 μs and 2 ms and maximal charge of 1 $mC/cm^2/phase$ were injected in trains of 20 trials at 0.1 Hz.

Figure 3.16a shows a 200 Hz high-passed filtered signal recorded by a 25 μm diameter microelectrode located 150 μm away from the stimulus origin when a 100 μs and 40 $\mu A/phase$ pulse was applied. There, the stimulation artifact could be identified t = 0 ms, and fast negative peaks were recognised again as spikes of RGCs after the stimulus was elicited. In this case, the PCA algorithm clustered those spikes only in one group, indicating that only one cell was being identified. The spike shape had similar features as before, occurring in times between 0.5 and 1 ms and reaching negative potentials of -70 μV (Figure 3.16b). The raster plot and PSTH in Figure 3.16 indicate that also the firing activity under this stimulus, was highly reproducible during the first 40 ms, occurring over the 20 trials at similar times. By gradually decreasing the current amplitude, the activity was maintained until 20 μA. Stimulation current amplitudes below that value resulted in absence neuronal response (Figures 3.16c and 3.16d). Calculating the firing probability then

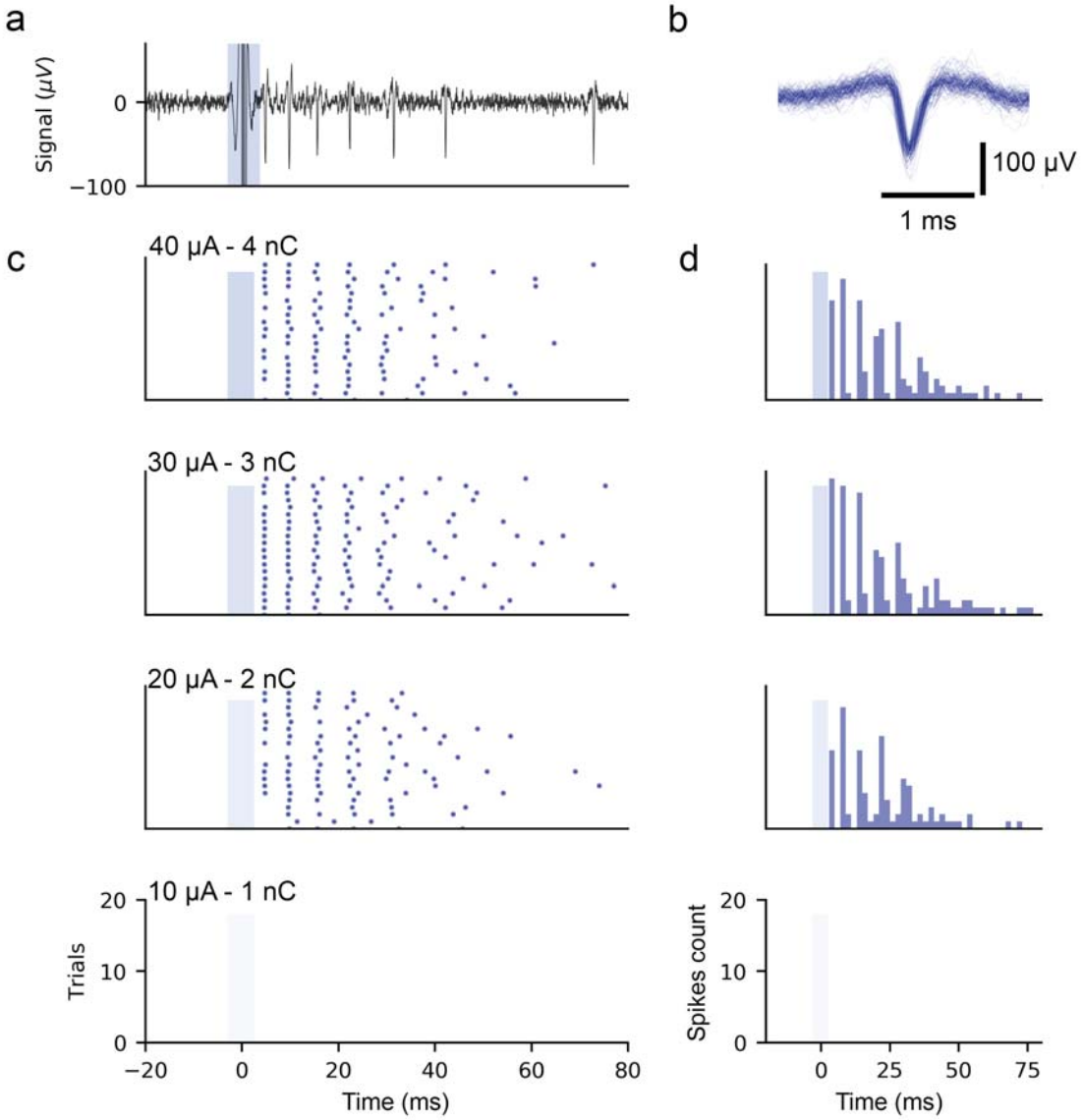

Figure 3.16: In vitro electrical stimulation of the retina using pulses of 500 μs pulsewidth. **a.** Electrical neural activity of the retinal tissue recorded with a 25 μm EGNITE electrode and high pass filtered at 200 Hz under biphasic, cathodic first, current-controlled pulse of 40 $\mu A/phase$ and 0.1 ms/phase (blue shadow). **b.** Wavelets overlap of the clustered neural activity. **c.** Raster plot with the activity of clustered activity obtained at different current amplitudes. **d.** Peri-stimulus time histogram (PSTH) of the clustered neural activity.

of the RGC, a sigmoid could be fitted to the data (Figure 3.17a). For pulses of 100 μs, the 50 % firing probability threshold was calculated to be 19.5 μA. Repeating this procedure for longer pulses of 500 μs, 1 ms and 2 ms, the strength-duration curve described in Section 1.2.4 was plotted for this specific neuron (Figure 3.17b). Equation 1.13 was fitted to the data, from which the rheobase current (I_{rh}) was

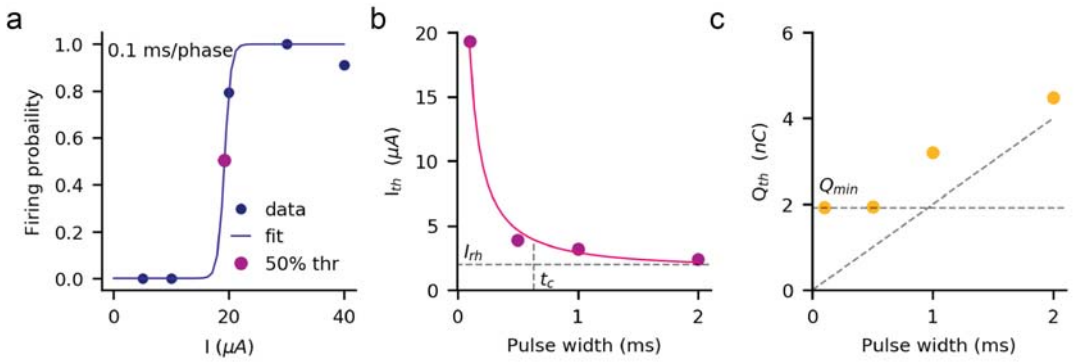

Figure 3.17: In vitro electrical stimulation threshold study. **a.** Firing probability of the RGC shown in Figure 3.16. **b.** Strength-duration curve, calculated from similar data to Figure 3.16 at longer pulse widths. **c.** Charge-duration curve, calculated from b.

derived to be 2 μA and the chronaxie (t_c) 630 μs. From this plot, the charge-duration curve was calculated. For pulses of 100 and 500 μs, the threshold charge was found to be 1.95 nC. For longer pulses, the necessary charge to elicit a response increased tending to $I_{rh}t$ curve. These results are consistent with previous literature, in which similar threshold values are reported for RGCs [148].

3.4.2 EGNITE technology for in vivo subretinal stimulation

To date, clinical retinal implants use MEA with the electrodes spaced more than 70 μm to modulate the activity of the RGC using the subretinal configuration, which results in a maximal vision acuity of 0.04 [142]. Improving this number requires smaller electrodes to focalise the stimulus in the retina on a more refined manner.

Here, we demonstrate the ability to stimulate in vivo the retina of a Long-Evans rat with 100, 50 and 25 μm diameter EGNITE electrodes and we examine the relation between the electrode dimensions and the area of brain activation as measured by functional ultrasound (fUS). fUS is an imaging technique that uses Doppler ultrasound to measure hemodynamic changes in the brain and from them, infer neural activity. For that, sound signals of frequencies in the MHz range are applied to the tissue and the ultrasensitive Doppler transducers detect the backscattered sound waves by the blood and permit to map the cerebral blood volume (CBV) over large cross sections of the brain with resolutions of up to 100 μm [149]. For the experiment, we subretinally implanted a flexible device that contained an EGNITE MEA and injected current controlled pulses into the tissue while the brain activity was being monitored by functional ultrasound (fUS) (Figure 3.18a)

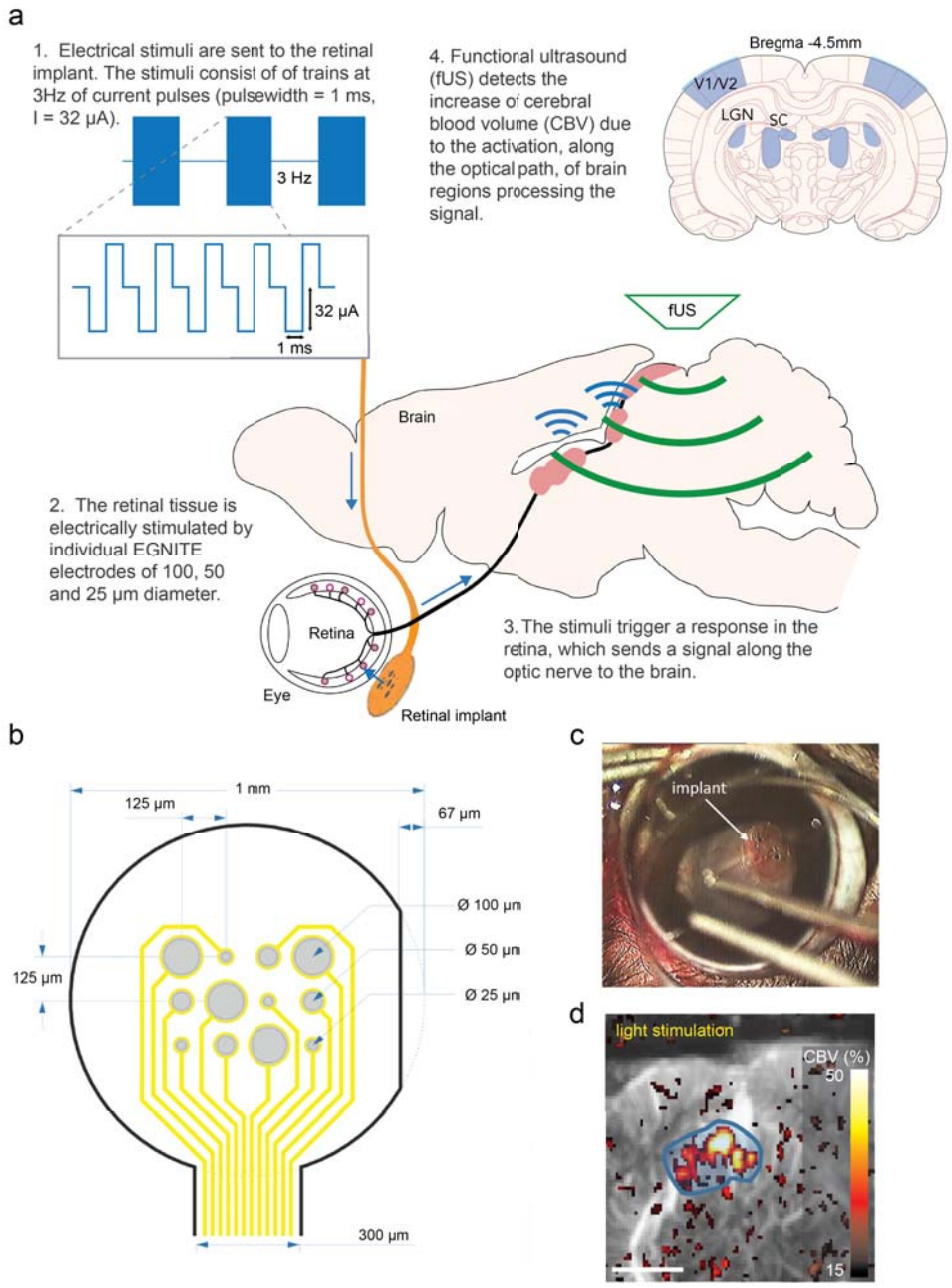

Figure 3.18: In vivo retinal stimulation setup. **a.** Schematic diagram of the in vivo retinal stimulation experiment. A flexible EGNITE MEA was implanted subretinally in a rat. Biphasic pulses of 1 ms/phase and an amplitude of 32 μA were injected in bursts at 3 Hz individually at the microelectrodes of 100, 50 and 25 μm diameter located in the device. The local electrical stimulation can depolarise the bipolar cells and RGCs from its vicinity and trigger an stimulus along the optic path to the brain, which processed the information in the Visual Cortex (V1/V2), Lateral Geniculate Nucleus (LGN) and Superior Colliculus (SC). The activity of those regions was monitored by functional ultrasound imaging. **b.** Schematics of the retinal implant device based on EGNITE used in this work. The device contained an array of 12 microelectrodes of 100, 50 and 25 μm diameter. **c.** Eye fundus image of the subretinally implanted EGNITE MEA. **d.** fUS imaging of the vision-induced activity at Bregma -4.5 mm, with superimposition of the correlated pixels (hot scale) over the brain vasculature (grey scale) during light stimulation. Scale bar = 2mm.

This way, we managed to monitor the activity of the optic path in the brain and correlate electrical stimuli with visual percepts. To fabricate the retinal implants we followed the procedure described in Section 2.2.0.1, but doubling the thickness of the substrate layer of polyimide, resulting in 24 μm thick devices, to mimic similar devices previously tested and to facilitate the implantation to the surgeon [150].

The active part of the device, of 1 mm wide, contained microelectrodes of 25, 50 and 100 μm diameter (Figure 3.18b). Figure 3.18c shows an eye fundus image of the EGNITE retinal device subretinally implanted. To electrically stimulate the tissue, current controlled biphasic pulses were injected in bursts of train pulses. The burst were delivered at 3 Hz for 100 times and the trains consisted of biphasic pulses of 1 ms/phase with an amplitude of 32 μA. This protocol was chosen in order to reproduce the conditions of previous works in which the activation of the optic path was recorded directly from the brain [150, 151]. The signals were individually injected through each of the microelectrodes of different sizes and for the smallest electrode, it corresponded to a charge density of 6.5 mC/cm^2. As a control, light stimulation was presented to the animal. The protocol followed was similar to the electrical stimulation pattern, in which the light was shined at 3 Hz in bursts that contained trains of light pulses of 1 ms duration [151]. To observe the brain activity, fUS monitored variations of the Cerebral Blood Volume (CBV) on a cross section of the brain in which the three regions responsible for the optic signal processing were aligned, i.e. the Superior Colliculus (SC) and the Lateral Geniculate Nuclei (LGN) and the visual cortices (V1/V2) [151]. For that, a CBV baseline of those regions was first recorded in the dark, with no activation of the optic path. This signal, was then substracted from the subsequent measurements in which optical activity was triggered, either with light or by electrical stimulation. From the data recorded then, influxes of blood above the baseline in the regions of the optic path correlated with processing of visual signals and thus, could be identified as visual percepts.

Figure 3.18d shows the CBV variation with respect to the baseline when the light stimulus was presented. Under these conditions, we assumed that most of the RGCs were being activated by the photoreceptors and assigned that signal to the maximal response [151]. From the three regions responsible for the optic signal processing, a response was only detected in the SC, registering a CBV increase of up to a 50 %. The area the signal covered was of 1.5 mm^2 as measured by fUS. We putatively attribute to a misaligned positioning of the fUS the fact that the other regions of interest showed no activity.

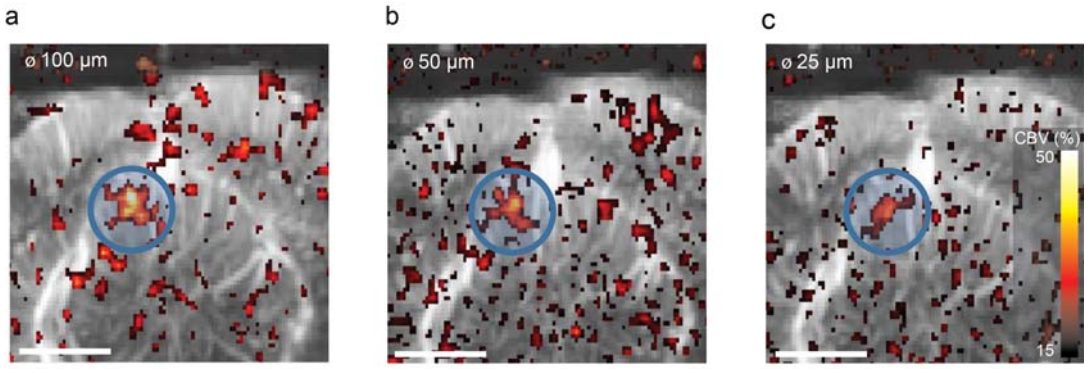

Figure 3.19: fUS imaging of the vision-induced activity at Bregma -4.5 mm, with superimposition of the correlated pixels (hot scale) over the brain vasculature (grey scale) during electrical stimulation using EGNITE microelectrodes of **a.** 100, **b.** 50 and **c.** 25 μm diameter. Scale bar = 2 mm.

Moving to electrical stimulation, Figure 3.19a, 3.19b and 3.19c show the CBV signal with respect to the baseline when the stimuli were applied through the 100, 50 and 25 μm diameter microelectrodes, respectively. In the three images a response was observed. However the extension of the signal and the CBV values significantly differed between the electrodes sizes. The large and the medium electrodes elicited a response on 0.78 mm^2 of the brain, while the small one reduced its influence to 0.43 mm^2 (Figure 3.20a). In terms of CBV variation, the 100 μm electrode registered a 30 % blood increase, followed by the 50 μm electrode with the 28 % and the 25 μm with a 25 % (Figure 3.20b).

The activation area registered in the brain is related to the area of the retina activated by the electric field pattern [152]. The larger the signal in the brain, the more the retinal cells had been previously activated. High vision acuity requires activating few and very localised retinal cells with high spatiotemporal resolution. In the case of the light stimulus, we assumed the signal to be maximal, with activation of most of the retinal cells and a prominent response in the SC [151, 152]. Electrical stimulation with single electrodes of 100 or 50 μm diameter, gave rise to signals that covered half the area the light was activating. When electrodes of 25 μm, were used, the signal extension reduced to 1 forth of the light stimulus and 50 % less CBV increase, which indicates that many less cells were activated, thus showing focal stimulation capabilities of such small EGNITE electrodes.

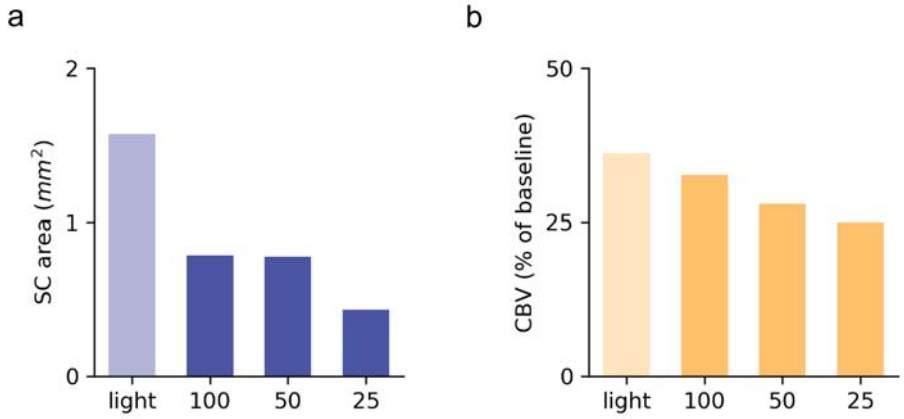

Figure 3.20: Functional ultrasound data analysis. **a.** Comparative plot of the SC area that exhibited correlated activity under the different kinds of stimuli **b.** Average Cerebral Blood Volume (CBV) variation with respect to the baseline in the SC regions that were activated.

This proof-of-concept experiment only aimed at proving the EGNITE capabilities for precise retinal stimulation. Future experiments should be carried out to explore the range of visual percepts that EGNITE microelectrodes of 25 μm diameter, or even less perhaps, can provide. Chronic stimulation and biocompatibility studies should also be performed to further validate the use of the technology in real applications. If successful, EGNITE technology could play an important role in the development of next generation retinal implants to restore vision with high resolution.

4

Conclusions and outlook

4.1 General conclusions

Neural implants offer therapeutic options to patients suffering from certain neurological disorders and other neural impairments (e.g. deafness [153], Parkinson's disease [154], amputations [114], etc.) [18, 38]. Such technology currently consists of implantable devices that either electrically record or stimulate the nervous system using millimetre-scale metallic electrodes [22]. To achieve broader acceptance of neural implants as a therapy, there is a need for a step-change improvement in their efficacy so that the therapeutic approach outweighs the risks from surgical implantation [23, 26, 30, 83, 155]. Increasing spatial neural interfacing resolution is at the core of such improvements [83, 156]. The millimetre scale of the electrodes partially limits the quality of the recorded neural activity and the precision of neural stimulation, which can limit the efficacy of the therapies. To improve the interface with the nervous system, the electrode dimensions should be in the micrometre-scale [18, 26, 114, 156].

Currently, the electrode size is limited by the metals used as electrodes, such as platinum (Pt) or iridium (Ir) [22, 73]. While these metallic interfaces can generally offer robust neural signal transduction when used in millimetre-scale electrodes, as the electrode size is reduced to the micrometre-scale, their performance dramatically drops due to their reduced electrochemical surface area, which increases the interfacial impedance and lowers the amount of charge that can be injected into the tissue [22]. This translates into noisy recordings with low signal-to-noise ratio (SNR) because

of the high contribution of the real part of the increased impedance. It also leads to the inability to stimulate the nervous tissue due to the combination of the low charge injection limit (CIL) of the metals and the reduced electrochemical surface area of the electrodes [22]. Another challenge with metal electrodes is that they electrically interface with the nervous tissue via a combination of faradaic and capacitive interactions. The presence of faradaic interactions is of great concern as they can change the pH of the media around them and dissolve the electrode into the tissue [22].

To address the inherent neural interfacing resolution and potential safety concerns associated with large metallic electrodes, high-performance materials have been explored to miniaturize neural interfaces [77]. Electrode surface modification strategies have been developed to increase the electrochemical surface area without increasing the geometric surface area of the electrode in order to improve the SNR and CIL of standard metal electrodes. To avoid faradaic reactions, materials whose interface in aqueous media is capacitive over a wide potential range, such as titanium nitride (TiN) or nanoporous boron-doped diamond, have been tested [79, 92]. However, TiN has been shown to exhibit low biocompatibility in certain cases [80] and the nanoporous boron-doped diamond has challenging fabrication constraints [92]. As an interesting alternative, conductive polymers (CP) such as poly(3,4-ethylenedioxythiophene) have been investigated in different combinations (PEDOT:PSS or PEDOT-CNT) due to their large electrochemical surface area, capacitive interface, and flexibility [81, 82]. However, the stability of these electrodes under continuous stimulation and in chronic settings remains debatable [83, 84].

Thus, currently there is not yet a robust and highly-biocompatible material that allows high-resolution and stable bidirectional neural interfacing.

This thesis presents the graphene-based EGNITE material as a promising candidate to create such bidirectional neural interfaces.

Chapter 2 describes the development of the EGNITE material, the technology to integrate it in flexible devices and the electrochemical performance and stability assessment of EGNITE microelectrodes when characterized in saline conditions. The main conclusions of Chapter 2 are the following:

- [redacted]

- [redacted]
- [redacted]
- [redacted]
- [redacted]

Further, we demonstrate a wafer-scale fabrication process of flexible neural probes for high spatial resolution neural recording and stimulation. The main conclusions from the technological development are:

- [redacted]
- [redacted]
- [redacted]
  - [redacted]

- [redacted]
  - [redacted]
- [redacted]
  - [redacted]

The successful fabrication of devices based on the EGNITE material, allowed us to perform electrochemical characterizations and stability studies of the fabricated microelectrodes in saline conditions. The main conclusions of such experiments are:

- [redacted]
  - [redacted]

- [redacted]
  - [redacted]
  - [redacted]
  - [redacted]
- [redacted]

In Chapter 3, we show preliminary biocompatibility results of the material and present proof-of-concept use of arrays of EGNITE microelectrodes (25 μm $\varnothing$) for in vivo epicortical recording, intraneural stimulation of nerve activity and retinal implants. Below are the main conclusions of the in vivo validation of the technology:

- Cell cultures grown on EGNITE substrates developed healthy and proliferated twice faster than on TCPS, the standard material used for cells incubation, indicating a very high biocompatibility of the material.
- The EGNITE microelectrodes exhibited intrinsic noise in the range of the best reported noise levels [30], allowing high SNR recordings of epicortical brain activity, even at high frequencies.
- During the intraneural stimulation study, the small diameter (25 μm) and high density of EGNITE electrodes permitted a very focal stimulation that increased the selectivity and lowered the charge-injection thresholds required for stimulation, when compared to the latest reports [115].
- Further, in vitro experiments with explanted retinas permitted to identify single neurons using basic spike sorting algorithms.

- In the case of the retinal neural interface, visual percepts were elicited by electrically stimulating the retina with electrodes significantly smaller than the ones currently used in clinical applications [142, 157].

Because of the conclusions above, and especially due to the promising results obtained in the in vitro performance and stability assessment and in the in vivo validation, we consider that the EGNITE technology we describe here has the potential to become the new performance benchmark for the next generation of high resolution neural implant technology. However, more experimentation is still necessary to fully demonstrate such potential.

4.2 Final remarks and outlook

Having presented in this thesis proof-of-concept demonstration of the possibilities that could be enabled by the EGNITE material and the technology associated to it, more extensive assessments are required to reach clinical applications [158].

Next, we present the steps that need to be performed to reach human applications.

- [redacted]
- [redacted]
- [redacted]
- [redacted]
- [redacted]

If those steps are successfully implemented, the combination of scalability, robustness and performance of the EGNITE technology has the potential to be used clinically for the next generation of neural implants providing safer and more efficient neuromodulation therapies. Next, we describe the ones we consider that EGNITE technology could potentiate the most:

- [redacted]
- [redacted]
- [redacted]
- [redacted]
- [redacted]

For all applications, the ethical implications of highly intimate interfaces with the nervous system need to be thoroughly considered [159, 160].

5 Appendix

5.1 Alternative distributed electric circuit model of the electrode

As an alternative model to describe the electrode it was considered a distribution of resistances and CPEs along the normal direction of the electrode material, which can be described as a transmission line of infinite height. Figure 5.1a shows a schematic of the model considered. Mathematically, the behavior of the potential U and the current I are described by the following equations [161]:

$$\frac{dI(z,t)}{dt} = -C_i \frac{dU(z,t)}{dt} \tag{5.1}$$

$$\frac{dU(z,t)}{dt} = -R_i I(z,t) \tag{5.2}$$

, where R_i and C_i are the resistance and the capacitance per unit length, respectively. By solving this set of equations, the characteristic impedance can be calculated to be:

$$Z_0 = \sqrt{\frac{R_i}{j\omega C_i}} \tag{5.3}$$

To fit this model to the impedance spectroscopy data of the EGNITE micro-electrode, an algorithm based on Python3 was custom-developed by extending the capabilities of the package PyEIS, designed to fit data from impedance measurements.

Figure 5.1b shows that the result obtained has severe discrepancies with the measured data, not being able to follow the curve at intermediate frequencies. Therefore, the results have to be taken with a grain of salt. The resistivity of the electrode material R_i was adjusted to 1 $G\Omega/cm$, the exponent of the CPE to 1 and the CPE value was set to 0.2 mF/cm^2. In this model, the signal decays over distance as $e^{-z/L}$, where L is the characteristic length of the system calculated as [161]:

$$L = 2\frac{Z_0}{R_i} \tag{5.4}$$

In this case for signals at 1 kHz L is calculated to be 8 μm. Therefore, in the case of the EGNITE electrodes, of only 2 μm thick, the entire bulk would be contributing to the charge injection. To improve the description of the material, we recommend to use a model that takes into account the electrode material in three dimensions.

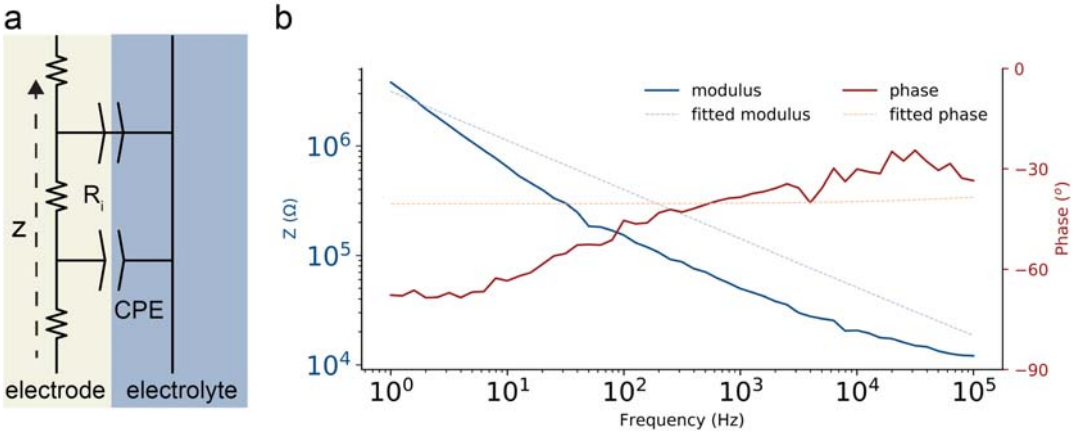

Figure 5.1: Alternative distributed model of the electrode. **a.** Distributed model, consisting of a transmission line with resistors and CPEs along the normal direction of the electrode. **b.** Fitting of the model to the measured impedance of an EGNITE microelectrode of 25 μm diameter. The model cannot capture the complexity of the measured data, but can extract its general trend.

5.2 EGNITE biocompatibility studies

Protein adsorption on substrates. Heat inactivated Foetal Bovine Serum (FBS; Sigma-Aldrich, Merck Sigma, UK) was drop-casted (150 µL) on four repeats of the different substrates (i.e. EGNITE; poly(3,4-ethylenedioxythiophene) polystyrene sulfonate, PEDOT:PSS, named hereafter PEDOT; or tissue culture polystyrene, TCPS). After 4 h incubation at room temperature, excess FBS was aspirated and the substrates were washed twice with PBS (Sigma-Aldrich, Merck Sigma, UK) to remove non-adsorbed proteins. Samples were then incubated at room temperature with 1 % Sodium Dodecyl Sulfate (Sigma-Aldrich, Merck Sigma, UK) in distilled water (Millipore, Merck, UK) for 30 min to desorb the adsorbed proteins. Total protein content was quantified according to manufacturer's instructions using a Pierce BCA Assay Kit (Thermo Fisher Scientific, UK) and a spectrophotometry plate reader (Fluostar Omega, BMG Labtech, UK) working at 562 nm for absorbance measurements.

Neuronal cell cultures. Human neuroblastoma cells (SH-SY5Y (ATCC® CRL-2266™), LGC standards, UK) were maintained in DMEM:F12 cell culture medium (Sigma-Aldrich, Merck Sigma, UK) supplemented with 20 mM glutamine (Sigma-Aldrich, Merck Sigma, UK), 10 % FBS (Gibco, Thermo Fisher Scientific, UK), 1000 units penicillin, and 1 mg/mL streptomycin (Sigma-Aldrich, Merck Sigma, UK) at 3^{o}C in a humidified 5% CO2 incubator (NuAire, USA). Cells were passaged twice a week using a 0.05 % TrypsinEDTA solution (Sigma-Aldrich, Merck Sigma, UK) when reaching 80 % confluence. All experiments were done using cells with a passage number below 20.

Cell viability assay. SHSY5Y cells were seeded at 50 000 cells per substrate (i.e. EGNITE; PEDOT; TCPS) in 12 well plate (1 mL final volume; Corning, USA). Positive controls for cell death were established by adding 10 % DMSO to the media of cells grown on TCPS wells. After 24 h of cell growth on the different substrates, sterile-filtered resazurin solution, obtained by dissolving resazurin sodium salt (Sigma-Aldrich, Merck Sigma,UK) in PBS to make a 0.15 mg.mL-1 (10 X solution), was added in each well to reach a 10 time dilution. Following 2 h incubation at 37 ^{o}C, 150 μL of the cell culture supernatants were transferred to black 96 well plates (Greiner Bio-one, Germany), whereas the remaining media was aspirated, cells were washed with PBS, fresh complete cell culture medium was added, and cells were incubated

at 37°C for the next time point. The fluorescence coming from the 96 well plates was measured using a Fluostar Omega plate reader (BMG Labtech, UK) at an excitation wavelength of 560 nm and emission of 590 nm. Fluorescence values were normalised to mean fluorescence for TCPS samples. After 48 h of cell growth on the different substrates, the same procedure was performed. The remaining cells at 48 h were used to performed cell counting (Trypan Blue assay).

Cytotoxicity assay. SHSY5Y cells were seeded at 50 000 cells per substrate (i.e. EGNITE, PEDOT, or TCPS) in 12 well plates (i.e. 1 mL final volume). DMSO 10 % added to cells grown on TCPS substrate was used as positive control in this assay. To assess cytotoxicity, a modified version of the Lactate DeHydrogenase (LDH) assay was performed (CytoTox 96 nonradioactive cytotoxicity assay, Promega LDH assay Kit). Briefly, supernatant media was aspirated, and cells were washed twice with PBS. Live cells at the bottom of the well were then lysed with 200 μL lysis solution (Triton X (Sigma Aldrich) at 0.9 % in water), 45 min at 37 ô C. Cell lysates (50 μL) was mixed 1:1 with LDH reaction solution. Mixtures were incubated for 15-20 min at room temperature until a steady red colour appears, before 50 μL of stop solution was added to each well. The absorbance of the wells was then measured at 490 nm using a Fluostar Omega plate reader (BMG Labtech, UK). The absorbance values were expressed relative to the TCPS controls.

Cell counting assay. SHSY5Y cells were seeded at 50 000 cells per substrate (i.e. EGNITE; PEDOT; TCPS) in 12 well plate (1 mL final volume; Corning, USA). DMSO 10 % added to cells grown on TCPS substrate was used as positive control in this assay. After 48 h of cell growth, supernatant was discarded and cells were washed twice with PBS (Sigma-Aldrich,Merck Sigma, UK), before a solution of trypsin-EDTA was applied (0.05 %; Sigma-Aldrich,Merck Sigma, UK) to detach the cells. An aliquot of the cell suspension was then mixed 1:1 with sterile solution of trypan blue (0.4 %; Thermo Fisher Scientific, UK), before cell counting was performed using an hemocytometer (BRAND counting chamber BLAUBRAND Neubauer improved).

Primary hippocampal neuron growth on EGNITE. Primary neuron cell cultures were prepared from hippocampus extracted from three-day old neonatal rat brain (REF Pacific). Sacrifice of the neonatal animals was performed in accordance with the UK Animals (Scientific Procedures) Act 1986 and the ARRIVE guidelines, following ethical approval from the UK Home Office, under Project License no. P089E2E0A. After determination of the number of live cells, cells were plated on

either glass coverslip or EGNITE, both pre-coated with 50 $\mu g/mL$ poly-L-lysine, at a density of 40 000 cells per substrate in serum-free neurobasal medium (Gibco, Thermo Fisher Scientific, UK) containing B27 supplement (Gibco, Thermo Fisher Scientific, UK), 1000 units penicillin and 1 mg/mL streptomycin (Sigma-Aldrich, Merck Sigma, UK), as well as 0.5 mM glutamine (Sigma-Aldrich, Merck Sigma,UK) for the first 3 days. Cultures were maintained at 37^{o}C in a humidified 5 % CO2 incubator (NuAire, USA) for 14 days; half of the volume of the wells was changed every three days.

Immunostaining of cells. After culture, both SHSY5Y and primary neurons were washed with PBS (Sigma-Aldrich, Merck Sigma, UK) three times before being fixed at room temperature for 10 min with 4 % PFA (Sigma-Aldrich, Merck Sigma, UK) in PBS. Then, fixed cells were permeabilized for 5 min with 0.1 % Triton X (Sigma-Aldrich, Merck Sigma, UK) diluted in PBS, before being blocked for 1 hour with 5 % PBS solution of goat serum (Sigma-Aldrich, Merck Sigma, UK). Cells were then incubated with a solution of primary antibodies for 2 h at room temperature (β-III Tubulin, ABCAM ab1827, Rabbit, used at 1:200). Following the incubation with primary antibodies, cells were washed three times with PBS, before being incubated for 1 h at room temperature with secondary antibodies (Anti-Rabbit conjugated with CY3, Jackson 111-165-144, used at 1:100). After staining, cells were thoroughly washed before being mounted with glass coverslips in Prolong Gold Antifade mountant containing DAPI (Invitrogen, Thermo Fisher Scientific, UK).

Microscopy imaging of β-III Tubulin immunoreactivity. Confocal Laser Scanning Microscopy was performed on a Zeiss LSM 880 (Systems Microscopy Centre, Manchester Bioimaging Facility, Faculty of Biology, Medicine and Health, the University of Manchester). Images were captured using a 1 AU pinhole and 2 % Laser power. Image processing was performed post-hoc using the Zeiss ZEN software package. Displayed images are a maximum intensity projection of 10 confocal slices; scale bars are 100 μm.

Statistical analysis. The Mann-Whitney U test using Graphpad Prism software was applied to all in vitro cell cultures assays. For all experiments, p values were displayed as: (*) $p < 0.05$; (**) $p< 0.01$; (***) $p < 0.005$; (****) $p < 0.0001$.

5.3 Surgical and animal procedures

Neural Recording. All experimental procedures were performed in accordance with the recommendations of the European Community Council and French legislation for care and use of laboratory animals. The protocols were approved by the Grenoble ethical committee (ComEth) and authorized by the French ministry (number 04815.02).

One Wister rate, weighing 200–350 g, was used. The rat was anesthetized intramuscularly with Ketamine (50 mg/kg) and Xylazine (10 mg/kg), and then fixed to a stereotaxic holder. Removing the temporal skull exposed the auditory cortex. Dura mater was preserved not to damage the cortical tissue. A hole was drilled at the vertex in order to insert the reference electrode and a second hole, 7 mm toward the front from the first one, in order to insert the ground electrode. The electrodes were 0.5-mm-thick pins used for integrated circuit sockets. They were placed to make electrical contacts with the dura mater and fixed to the skull with dental cement. We then mounted the surface microelectrode ribbon on the auditory cortex as Figure 4b shows. The vein patterns identify the auditory cortex, in area 41 of Krieg's rat brain map: that is, posterior to an ascending branch of the inferior cerebral vein in the caudal part of the temporal cortex.

Cortical signals were simultaneously amplified with a gain of 1000 and filtered with a band-pass of 20 Hz–1500 Hz, 12 dB/octave, and digitized at a sampling rate of 20 s. A speaker 20 cm in front of a rats' ear, contra-lateral to the exposed cortex, delivered acoustic stimuli. The stimuli delivered were monitored by a 1/4-in microphone (Bruel & Kjaer, 4939) placed near the ear and presented in sound pressure level (dB SPL re 20 Pa). We examine the vertex-positive (negative up) MLRs, evoked by alternating clicks at 80-dB SPL, and tone burst stimuli at 70-dB SPL with the frequencies ranging 5 kHz–40 kHz, the rise and fall time of 5 ms and the duration of 200 ms. These data presented show the average after taking 100 trials.

Neural Stimulation - sciatic nerve. All animal experiments were approved by the Ethical Committee of the Universitat Autònoma de Barcelona in accordance with the European Communities Council Directive 2010/63/EU. Animals were housed at 22±2ºC under a 12:12h light cycle with food and water ad libitum. The sciatic nerve of anesthetized Sprague-Dawley rats (250-300g) was surgically exposed and the nerve electrodes were implanted transversally across the sciatic nerve with the help of a

straight needle attached to a 10-0 loop thread [116]. The process was monitored under a dissection microscope to ensure the correct position of the active sites inside the nerve fascicles. During the experiments the animal body temperature was maintained by means of a thermostated heating pad. After the electrophysiological test, the electrodes were collected and stored for further in vitro characterization.

Nerve stimulation was performed by applying trains of biphasic current pulses of a fixed duration of 100 µs and increasing amplitude from 0 to 100 μA (STG 4002, Multichannel System GmbH) through the different EGNITE microelectrodes. Simultaneously, the CMAPs were recorded from GM, TA and PL muscles using small needle electrodes placed in each muscle; the active electrode on the muscle belly and the reference at the level of the tendon. Electromyography (EMG) recordings were amplified (P511AC amplifiers, Grass), band-pass filtered (3 Hz to 3 kHz) and digitized with a Powerlab recording system (PowerLab16SP, ADInstruments) at 20 kHz. The amplitude of each CMAP was measured from baseline to the maximum negative peak. The voltage peak measurements were normalized to the maximum CMAP amplitude obtained for each muscle in the experiment. A selectivity index (SI) was calculated as the ratio between the normalized CMAP amplitude for one muscle, CMAPi, and the sum of the normalized CMAP amplitudes in the three muscles, following the formula $SI_i = nCMAP_i / \sum nCMAP_j$.

Neural Stimulation - in vitro retina. Royal college of surgeon rats were sacrificed with approval from the Charles Darwin No5 Ethics Committee in Animal Experimentation by CO2-inhalation and cervical dislocation. The eyes were immediately removed and placed in Ames' Medium buffered with sodium bicarbonate and continuously oxygenated with a 95 % O2 / 5 % CO2 gas mixture. Retinas were dissected from the eye while in the media. The vitreous was removed from the retina before mounting the retina on the microelectrode array. The retina was placed ganglion cell side down on the MEA and held gently in contact with the MEA using a weighted nylon mesh. The retina was continuously perfused (2 mL/min) with fresh oxygenated Ames' Medium and maintained at 30 ^{o}C throughout the experiment.

Neural Stimulation - in vivo retina. Sighted, Long-Evans rats, aged 3 -12 months were implanted with approval from the Charles Darwin No5 Ethics Committee in Animal Experimentation. Rats were anesthetized with 5 % isoflourane, and then a cocktail of ketamine (60 mg/kg Imalgene1000, Merial, FR) and meditomedine (0.4 mg/kg Domitor, Pfizer, Sante) injected via intraperitoneal. The anesthesia was

maintained by IP injection of 1/3 initial volume each 45 minutes. The animal was placed on a heating platform to maintain body temperature of 37 ^{o}C. Craniotomy was performed aided by a stereotaxic frame with local anesthesia by xylocaine.

For the subretinal implantation of the electrodes the eye was first dilated using mydriaticum. Then, a small sclerotomy was made tangential to the cornea on the dorsal sclera and 1 mm incision on the sclera was carried out. Hydrodissection with balanced saline solution (BSS) was used to temporarily separate the retina from the retinal pigmented epithelium [152]. The active site of the implants was inserted into the subretinal space and positioned close to the fovea which was confirmed by surgical microscope (Figure 3.18c) [150].

For the craniotomy to perform the functional ultrasound (fUS) imaging, a sagittal skin incision was performed across the posterior part of the head to expose the skull. Parietal bone were removed by drilling rectangular flaps and gently moving the bone away from the dura mater. Thus exposing the cortex over the visual cortex from Bregma -4 to Bregma -7 mm, with a maximal width of 14 mm.

The animals were kept under dark conditions from the beginning of the surgery to the stimuli trials. The surgery lasting about an hour, animals can be considered to be dark-adapted.

Light visual stimuli were delivered using a 51×29 cm^2, 1920×1080 pixels screen (P2314H 23", Dell), in front of the rat at 8 cm, therefore covering 145° of the visual field in the horizontal dimension and about 122° in the vertical dimension. At 8 cm, we measured a maximum luminance of 8 cd/m^2 (full white screen) and a minimum luminance of 0.04 cd/m^2 (full black screen). Stimulation runs consist in episodic presentations of black and white flickering on the screen interleaved with black screen period for rest: A run consisted in 30 s of rest followed by 30 s of flicker repeated 5 times and ended with 30 s of rest for a total duration of 330 s. The stimuli were designed and displayed using Matlab (Psychtoolbox-3, Mathworks, Natick, Massachusetts, USA). Between stimuli presentation sessions, the rats were kept in a dark environment. The electrical connection between the EGNITE MEA and the stimulator (STG-4002 Multichannel Systems GmbH) was made using an Omnetics 18-position nanominiature connector.

fUS imaging was performed using a linear ultrasound probe (128 elements, 15 MHz, 110 μm pitch and 8 mm elevation focus, Vermon; Tours, France) driven by an ultrafast ultrasound scanner (Aixplorer, Supersonic Imagine; Aix-en-Provence, France).

5.4 Data Analysis

Physicochemical, electrochemical and neural data were analysed using Python 2.7 packages (Matplotlib, Numpy, Rampy, xrdtools, PyEIS, Neo, sklearn) and the custom library PhyREC.

References

[1] Michael Okuda and Denise Okuda. *The Star Trek Encyclopedia, Revised and Expanded Edition: A Reference Guide to the Future*. en. HarperCollins, Oct. 2016.

[2] Judith A Westman. *Medical Genetics for the Modern Clinician*. en. Lippincott Williams & Wilkins, 2006.

[3] J C Venter et al. "The sequence of the human genome". en. In: *Science* 291.5507 (Feb. 2001), pp. 1304–1351.

[4] Sarah Mack et al. *Principles of Neural Science, Fifth Edition*. en. McGraw Hill Professional, 2013.

[5] Katrin Amunts et al. "The Human Brain Project: Creating a European Research Infrastructure to Decode the Human Brain". en. In: *Neuron* 92.3 (Nov. 2016), pp. 574–581.

[6] Henry Markram. "The human brain project". en. In: *Sci. Am.* 306.6 (June 2012), pp. 50–55.

[7] Allan R Jones, Caroline C Overly, and Susan M Sunkin. "The Allen Brain Atlas: 5 years and beyond". en. In: *Nat. Rev. Neurosci.* 10.11 (Nov. 2009), pp. 821–828.

[8] Terri L Gilbert and Lydia Ng. "Chapter 3 - The Allen Brain Atlas: Toward Understanding Brain Behavior and Function Through Data Acquisition, Visualization, Analysis, and Integration". In: *Molecular-Genetic and Statistical Techniques for Behavioral and Neural Research*. Ed. by Robert T Gerlai. San Diego: Academic Press, Jan. 2018, pp. 51–72.

[9] Lyric A Jorgenson et al. "The BRAIN Initiative: developing technology to catalyse neuroscience discovery". en. In: *Philos. Trans. R. Soc. Lond. B Biol. Sci.* 370.1668 (May 2015).

[10] Aravi Samuel, Herbert Levine, and Krastan B Blagoev. “Scientific priorities for the BRAIN Initiative”. en. In: *Nat. Methods* 10.8 (Aug. 2013), pp. 713–714.

[11] Meghan C Mott, Joshua A Gordon, and Walter J Koroshetz. “The NIH BRAIN Initiative: Advancing neurotechnologies, integrating disciplines”. en. In: *PLoS Biol.* 16.11 (Nov. 2018), e3000066.

[12] Cornelia I Bargmann and Jeffrey A Lieberman. “What the BRAIN Initiative means for psychiatry”. en. In: *Am. J. Psychiatry* 171.10 (Oct. 2014), pp. 1038–1040.

[13] Sung-Jin Jeong et al. “Korea Brain Initiative: Integration and Control of Brain Functions”. en. In: *Neuron* 92.3 (Nov. 2016), pp. 607–611.

[14] Rafael Yuste and Cori Bargmann. “Toward a Global BRAIN Initiative”. en. In: *Cell* 168.6 (Mar. 2017), pp. 956–959.

[15] Shaun R Patel and Charles M Lieber. “Precision electronic medicine in the brain”. en. In: *Nat. Biotechnol.* 37.9 (Sept. 2019), pp. 1007–1012.

[16] Steven M Wellman et al. “A Materials Roadmap to Functional Neural Interface Design”. In: *Adv. Funct. Mater.* (2017).

[17] James A Frank, Marc-Joseph Antonini, and Polina Anikeeva. “Next-generation interfaces for studying neural function”. en. In: *Nat. Biotechnol.* 37.9 (Sept. 2019), pp. 1013–1023.

[18] David Zhou and Elias Greenbaum, eds. *Implantable Neural Prostheses 2: Techniques and Engineering Approaches*. Springer, New York, NY, 2010.

[19] Robert K Shepherd. *Neurobionics: The Biomedical Engineering of Neural Prostheses*. en. John Wiley & Sons, Aug. 2016.

[20] Horch Kenneth W and Kipke Daryl R. *Neuroprosthetics: Theory And Practice (Second Edition)*. en. World Scientific, Mar. 2017.

[21] Elliot Krames, P Hunter Peckham, and Ali R Rezai. *Neuromodulation: Comprehensive Textbook of Principles, Technologies, and Therapies*. en. Academic Press, Jan. 2018.

[22] Stuart F Cogan. “Neural Stimulation and Recording Electrodes”. In: *Annu. Rev. Biomed. Eng.* 10.1 (2008), pp. 275–309.

[23] Gopala K Anumanchipalli, Josh Chartier, and Edward F Chang. “Speech synthesis from neural decoding of spoken sentences”. In: *Nature* (2019).

[24] Henri Lorach et al. “Photovoltaic restoration of sight with high visual acuity”. In: *Nat. Med.* 21.5 (2015), pp. 476–482.

[25] Philip M Lewis et al. “Advances in implantable bionic devices for blindness: a review”. en. In: *ANZ J. Surg.* 86.9 (Sept. 2016), pp. 654–659.

[26] Xavier Navarro et al. “A critical review of interfaces with the peripheral nervous system for the control of neuroprostheses and hybrid bionic systems”. en. In: *J. Peripher. Nerv. Syst.* 10.3 (Sept. 2005), pp. 229–258.

[27] Elon Musk and Neuralink. “An integrated brain-machine interface platform with thousands of channels”. In: *bioRxiv* (2019).

[28] Xiao Yang et al. “Bioinspired neuron-like electronics”. In: *Nat. Mater.* (2019).

[29] Gopala K Anumanchipalli, Josh Chartier, and Edward F Chang. “Speech synthesis from neural decoding of spoken sentences”. In: *Nature* (2019).

[30] Dion Khodagholy et al. “NeuroGrid: Recording action potentials from the surface of the brain”. In: *Nat. Neurosci.* 18.2 (2015), pp. 310–315.

[31] Kristoffer Famm et al. “A jump-start for electroceuticals”. In: *Nature* (2013).

[32] Valentin A Pavlov and Kevin J Tracey. “Bioelectronic medicine: updates, challenges and paths forward”. In: *Bioelectronic Medicine* (2019).

[33] Karen Birmingham et al. “Bioelectronic medicines: a research roadmap”. en. In: *Nat. Rev. Drug Discov.* 13.6 (June 2014), pp. 399–400.

[34] Warren M Grill, Sharon E Norman, and Ravi V Bellamkonda. “Implanted neural interfaces: biochallenges and engineered solutions”. en. In: *Annu. Rev. Biomed. Eng.* 11 (2009), pp. 1–24.

[35] Ernst Niedermeyer and F H Lopes da Silva. *Electroencephalography: Basic Principles, Clinical Applications, and Related Fields*. en. Lippincott Williams & Wilkins, 2005.

[36] Abraham Kuruvilla and Roland Flink. “Intraoperative electrocorticography in epilepsy surgery: useful or not?” en. In: *Seizure* 12.8 (Dec. 2003), pp. 577–584.

[37] Eran Stark and Moshe Abeles. “Predicting movement from multiunit activity”. en. In: *J. Neurosci.* 27.31 (Aug. 2007), pp. 8387–8394.

[38] Kenneth W Horch and Gurpreet S Dhillon. *Neuroprosthetics Theory and Practice*. 2004.

[39] Or A Shemesh et al. “Temporally precise single-cell-resolution optogenetics”. en. In: *Nat. Neurosci.* 20.12 (Dec. 2017), pp. 1796–1806.

[40] Karl Deisseroth. “Optogenetics”. en. In: *Nat. Methods* 8.1 (Jan. 2011), pp. 26–29.

[41] Xin Fu et al. “Clinical applications of retinal gene therapies”. In: *Prec Clin Med* 1.1 (June 2018), pp. 5–20.

[42] Juliette E McGregor et al. “Optogenetic restoration of retinal ganglion cell activity in the living primate”. en. In: *Nat. Commun.* 11.1 (Apr. 2020), p. 1703.

[43] Allen J Bard et al. *Electrochemical methods: fundamentals and applications*. Vol. 2. wiley New York, 1980.

[44] Evgenij Barsoukov and J Ross Macdonald. *Impedance Spectroscopy: Theory, Experiment, and Applications*. en. John Wiley & Sons, Apr. 2005.

[45] Simon Drieschner et al. “Frequency response of electrolyte-gated graphene electrodes and transistors”. en. In: *J. Phys. D Appl. Phys.* 50.9 (Feb. 2017), p. 095304.

[46] Hubert H Girault. *Analytical and Physical Electrochemistry*. en. EPFL Press, Oct. 2004.

[47] Jong Min Ong and Lyndon da Cruz. *The bionic eye: A review*. 2012.

[48] Guosong Hong and Charles M Lieber. “Novel electrode technologies for neural recordings”. en. In: *Nat. Rev. Neurosci.* 20.6 (June 2019), pp. 330–345.

[49] Louis Lapicque. “Recherches quantitatives sur l’excitation électrique des nerfs traitée comme une polarisation”. In: *J. Physiol. Pathol. Gen.* 9 (1907), pp. 620–635.

[50] H Bostock. “The strength-duration relationship for excitation of myelinated nerve: computed dependence on membrane parameters”. In: *J. Physiol.* 341.1 (1983), pp. 59–74.

[51] L A Geddes and J D Bourland. “The strength-duration curve”. en. In: *IEEE Trans. Biomed. Eng.* 32.6 (June 1985), pp. 458–459.

[52] I Mogyoros, M C Kiernan, and D Burke. “Strength-duration properties of human peripheral nerve”. en. In: *Brain* 119 (Pt 2) (Apr. 1996), pp. 439–447.

[53] D C West and J H Wolstencroft. “Strength-duration characteristics of myelinated and non-myelinated bulbospinal axons in the cat spinal cord”. en. In: *J. Physiol.* 337 (Apr. 1983), pp. 37–50.

[54] E N Warman, W M Grill, and D Durand. “Modeling the effects of electric fields on nerve fibers: determination of excitation thresholds”. en. In: *IEEE Trans. Biomed. Eng.* 39.12 (Dec. 1992), pp. 1244–1254.

[55] Robert Plonsey and Roger C Barr. *Bioelectricity: A Quantitative Approach*. en. Springer Science & Business Media, May 2007.

[56] A L Hodgkin and A F Huxley. “A quantitative description of membrane current and its application to conduction and excitation in nerve”. en. In: *J. Physiol.* 117.4 (Aug. 1952), pp. 500–544.

[57] Po-Min Wang et al. “A Novel Biomimetic Stimulator System for Neural Implant”. en. In: *Int. IEEE EMBS Conf. Neural Eng.* 2019 (Mar. 2019), pp. 843–846.

[58] R V Shannon. “A model of safe levels for electrical stimulation”. en. In: *IEEE Trans. Biomed. Eng.* 39.4 (Apr. 1992), pp. 424–426.

[59] Stuart F Cogan et al. “Tissue damage thresholds during therapeutic electrical stimulation”. In: *J. Neural Eng.* (2016).

[60] Doe W Kumsa et al. “Electron transfer processes occurring on platinum neural stimulating electrodes: pulsing experiments for cathodic-first/charge-balanced/biphasic pulses for $0.566 \leq k \leq 2.3$ in oxygenated and deoxygenated sulfuric acid”. en. In: *J. Neural Eng.* 13.5 (Oct. 2016), p. 056001.

[61] Raymond M Bonnet et al. “Effects of pulse width, pulse rate and paired electrode stimulation on psychophysical measures of dynamic range and speech recognition in cochlear implants”. en. In: *Ear Hear.* 33.4 (July 2012), pp. 489–496.

[62] Clara Günter, Jean Delbeke, and Max Ortiz-Catalan. “Safety of long-term electrical peripheral nerve stimulation: review of the state of the art”. en. In: *J. Neuroeng. Rehabil.* 16.1 (Jan. 2019), p. 13.

[63] Mark H Histed, Vincent Bonin, and R Clay Reid. “Direct activation of sparse, distributed populations of cortical neurons by electrical microstimulation”. en. In: *Neuron* 63.4 (Aug. 2009), pp. 508–522.

[64] S B Brummer and M J Turner. “Electrical stimulation with Pt electrodes: II-estimation of maximum surface redox (theoretical non-gassing) limits”. en. In: *IEEE Trans. Biomed. Eng.* 24.5 (Sept. 1977), pp. 440–443.

[65] T L Rose and L S Robblee. “Electrical stimulation with Pt electrodes. VIII. Electrochemically safe charge injection limits with 0.2 ms pulses”. en. In: *IEEE Trans. Biomed. Eng.* 37.11 (Nov. 1990), pp. 1118–1120.

[66] T L Rose, E M Kelliher, and L S Robblee. “Assessment of capacitor electrodes for intracortical neural stimulation”. en. In: *J. Neurosci. Methods* 12.3 (Jan. 1985), pp. 181–193.

[67] György Buzsáki, Costas A Anastassiou, and Christof Koch. “The origin of extracellular fields and currents–EEG, ECoG, LFP and spikes”. en. In: *Nat. Rev. Neurosci.* 13.6 (May 2012), pp. 407–420.

[68] P J Rousche and R A Normann. “Chronic recording capability of the Utah Intracortical Electrode Array in cat sensory cortex”. en. In: *J. Neurosci. Methods* 82.1 (July 1998), pp. 1–15.

[69] Vijay Viswam et al. “Optimal Electrode Size for Multi-Scale Extracellular-Potential Recording From Neuronal Assemblies”. en. In: *Front. Neurosci.* 13 (Apr. 2019), p. 385.

[70] *The Axon Guide for Electrophysiology & Biophysics Laboratory Techniques*. en. Axon Instruments, 1993.

[71] A H Flasterstein. “Voltage fluctuations of metal-electrolyte interfaces in electrophysiology”. en. In: *Med. Biol. Eng.* 4.6 (Nov. 1966), pp. 583–588.

[72] Daniel R Merrill. “The Electrochemistry of Charge Injection at the Electrode/Tissue Interface”. In: *Implantable Neural Prostheses 2: Techniques and Engineering Approaches*. Ed. by David Zhou and Elias Greenbaum. New York, NY: Springer New York, 2010, pp. 85–138.

[73] C Henle et al. “Electrical Characterization of Platinum, Stainless Steel and Platinum/Iridium as Electrode Materials for a New Neural Interface”. In: *World Congress on Medical Physics and Biomedical Engineering, September 7 - 12, 2009, Munich, Germany*. Springer Berlin Heidelberg, 2009, pp. 100–103.

[74] Jia Liu et al. “Syringe-injectable electronics”. en. In: *Nat. Nanotechnol.* 10.7 (July 2015), pp. 629–636.

[75] Guosong Hong et al. “Mesh electronics: a new paradigm for tissue-like brain probes”. en. In: *Curr. Opin. Neurobiol.* 50 (June 2018), pp. 33–41.

[76] Thomas G Schuhmann Jr et al. “Syringe-injectable Mesh Electronics for Stable Chronic Rodent Electrophysiology”. en. In: *J. Vis. Exp.* 137 (July 2018).

[77] Matthias Heim, Blaise Yvert, and Alexander Kuhn. “Nanostructuration strategies to enhance microelectrode array (MEA) performance for neuronal recording and stimulation”. en. In: *J. Physiol. Paris* 106.3-4 (May 2012), pp. 137–145.

[78] Sejin Park et al. “Nanoporous Pt Microelectrode for Neural Stimulation and Recording: In Vitro Characterization”. In: *J. Phys. Chem. C* 114.19 (May 2010), pp. 8721–8726.

[79] Naser Pour Aryan et al. “In vitro study of titanium nitride electrodes for neural stimulation”. en. In: *Conf. Proc. IEEE Eng. Med. Biol. Soc.* 2011 (2011), pp. 2866–2869.

[80] E Guenther et al. “Long-term survival of retinal cell cultures on retinal implant materials”. en. In: *Vision Res.* 39.24 (Dec. 1999), pp. 3988–3994.

[81] Ramona Gerwig et al. “PEDOT–CNT Composite Microelectrodes for Recording and Electrostimulation Applications: Fabrication, Morphology, and Electrical Properties”. In: *Front. Neuroeng.* 5 (2012).

[82] Takao Someya, Zhenan Bao, and George G Malliaras. “The rise of plastic bioelectronics”. en. In: *Nature* 540.7633 (Dec. 2016), pp. 379–385.

[83] Elon Musk and Neuralink. “An Integrated Brain-Machine Interface Platform With Thousands of Channels”. en. In: *J. Med. Internet Res.* 21.10 (Oct. 2019), e16194.

[84] Seth J Wilks et al. “Poly(3,4-ethylenedioxythiophene) as a Micro-Neural Interface Material for Electrostimulation”. In: *Front. Neuroeng.* 2 (June 2009), p. 7.

[85] N More et al. “Biocompatibility of carbon-carbon materials: in vivo study of their erosion using 14carbon labelled samples”. en. In: *Biomaterials* 9.4 (July 1988), pp. 328–334.

[86] Richard Petersen. “Carbon Fiber Biocompatibility for Implants”. en. In: *Fibers (Basel)* 4.1 (Jan. 2016).

[87] Linlin Lu et al. “Soft and MRI Compatible Neural Electrodes from Carbon Nanotube Fibers”. en. In: *Nano Lett.* 19.3 (Mar. 2019), pp. 1577–1586.

[88] Surabhi Nimbalkar et al. “Glassy carbon microelectrodes minimize induced voltages, mechanical vibrations, and artifacts in magnetic resonance imaging”. en. In: *Microsyst Nanoeng* 5 (Nov. 2019), p. 61.

[89] Maria Vomero et al. “Highly Stable Glassy Carbon Interfaces for Long-Term Neural Stimulation and Low-Noise Recording of Brain Activity”. en. In: *Sci. Rep.* 7 (Jan. 2017), p. 40332.

[90] Surabhi Nimbalkar et al. “Ultra-Capacitive Carbon Neural Probe Allows Simultaneous Long-Term Electrical Stimulations and High-Resolution Neurotransmitter Detection”. en. In: *Sci. Rep.* 8.1 (May 2018), p. 6958.

[91] Maria Vomero et al. “Glassy Carbon Electrocorticography Electrodes on Ultra-Thin and Finger-Like Polyimide Substrate: Performance Evaluation Based on Different Electrode Diameters”. en. In: *Materials* 11.12 (Dec. 2018).

[92] Gaëlle Piret et al. “3D-nanostructured boron-doped diamond for microelectrode array neural interfacing”. In: *Biomaterials* 53 (2015), pp. 173–183.

[93] S K Smart et al. “The biocompatibility of carbon nanotubes”. In: *Carbon N. Y.* 44.6 (May 2006), pp. 1034–1047.

[94] Swati Sharma. “Glassy Carbon: A Promising Material for Micro- and Nanomanufacturing”. en. In: *Materials* 11.10 (Sept. 2018).

[95] Mattia Bramini et al. “Neuronal Cultures and Nanomaterials”. en. In: *Adv Neurobiol* 22 (2019), pp. 51–79.

[96] Farid Menaa, Adnane Abdelghani, and Bouzid Menaa. “Graphene nanomaterials as biocompatible and conductive scaffolds for stem cells: impact for tissue engineering and regenerative medicine”. en. In: *J. Tissue Eng. Regen. Med.* 9.12 (Dec. 2015), pp. 1321–1338.

[97] John O’brien et al. “Investigation of the Alamar Blue (resazurin) fluorescent dye for the assessment of mammalian cell cytotoxicity”. In: *Eur. J. Biochem.* 267.17 (2000), pp. 5421–5426.

[98] Ronald P Lesser, Nathan E Crone, and W R S Webber. “Subdural electrodes”. en. In: *Clin. Neurophysiol.* 121.9 (Sept. 2010), pp. 1376–1392.

[99] Andreas K Engel et al. “Invasive recordings from the human brain: clinical insights and beyond”. en. In: *Nat. Rev. Neurosci.* 6.1 (Jan. 2005), pp. 35–47.

[100] F Sebastiano et al. “A rapid and reliable procedure to localize subdural electrodes in presurgical evaluation of patients with drug-resistant focal epilepsy”. en. In: *Clin. Neurophysiol.* 117.2 (Feb. 2006), pp. 341–347.

[101] Jinxian Yuan, Yangmei Chen, and Edouard Hirsch. “Intracranial electrodes in the presurgical evaluation of epilepsy”. en. In: *Neurol. Sci.* 33.4 (Aug. 2012), pp. 723–729.

[102] P Jayakar, M Duchowny, and T J Resnick. “Subdural monitoring in the evaluation of children for epilepsy surgery”. en. In: *J. Child Neurol.* 9 Suppl 2 (Oct. 1994), pp. 61–66.

[103] P G Matz, C Cobbs, and M S Berger. “Intraoperative cortical mapping as a guide to the surgical resection of gliomas”. en. In: *J. Neurooncol.* 42.3 (May 1999), pp. 233–245.

[104] Hugues Duffau. “Brain mapping in tumors: intraoperative or extraoperative?” en. In: *Epilepsia* 54 Suppl 9 (Dec. 2013), pp. 79–83.

[105] Javier Nieto-Diego and Manuel S Malmierca. “Topographic Distribution of Stimulus-Specific Adaptation across Auditory Cortical Fields in the Anesthetized Rat”. en. In: *PLoS Biol.* 14.3 (Mar. 2016), e1002397.

[106] D P Philips and D R F Irvine. “Responses of single neurons in physiologically defined area A1 of cat cerebral cortex: senitivity to interaural intensity differences”. In: *Hear. Res.* 4.3-4 (1981), pp. 299–307.

[107] T M McKenna et al. “Muscarinic agonists modulate spontaneous and evoked unit discharge in auditory cortex of cat”. en. In: *Synapse* 2.1 (1988), pp. 54–68.

[108] György Buzsáki, Costas A Anastassiou, and Christof Koch. “The origin of extracellular fields and currents–EEG, ECoG, LFP and spikes”. en. In: *Nat. Rev. Neurosci.* 13.6 (May 2012), pp. 407–420.

[109] Panagiotis C Petrantonakis and Panayiota Poirazi. “A Novel and Simple Spike Sorting Implementation”. en. In: *IEEE Trans. Neural Syst. Rehabil. Eng.* 25.4 (Apr. 2017), pp. 323–333.

[110] Sohmyung Ha et al. *High-Density Integrated Electrocortical Neural Interfaces: Low-Noise Low-Power System-on-Chip Design Methodology*. en. Academic Press, Aug. 2019.

[111] Alex Suarez-Perez et al. “Quantification of signal-to-noise ratio in cerebral cortex recordings using flexible MEAs with co-localized platinum black, carbon nanotubes, and gold electrodes”. In: *Front. Neurosci.* 12 (2018), p. 862.

[112] W Schady et al. “Responsiveness of the somatosensory system after nerve injury and amputation in the human hand”. en. In: *Ann. Neurol.* 36.1 (July 1994), pp. 68–75.

[113] P Marchettini, M Cline, and J L Ochoa. “Innervation territories for touch and pain afferents of single fascicles of the human ulnar nerve. Mapping through intraneural microrecording and microstimulation”. en. In: *Brain* 113 (Pt 5) (Oct. 1990), pp. 1491–1500.

[114] Stanisa Raspopovic et al. “Restoring natural sensory feedback in real-time bidirectional hand prostheses”. en. In: *Sci. Transl. Med.* 6.222 (Feb. 2014), 222ra19.

[115] N de la Oliva et al. “Long-Term Functionality of Transversal Intraneural Electrodes Is Improved By Dexamethasone Treatment”. en. In: *IEEE Trans. Neural Syst. Rehabil. Eng.* (Feb. 2019).

[116] Tim Boretius et al. “A transverse intrafascicular multichannel electrode (TIME) to interface with the peripheral nerve”. en. In: *Biosens. Bioelectron.* 26.1 (Sept. 2010), pp. 62–69.

[117] Tim Boretius et al. “A transverse intrafascicular multichannel electrode (TIME) to treat phantom limb pain—Towards human clinical trials”. In: *2012 4th IEEE RAS & EMBS International Conference on Biomedical Robotics and Biomechatronics (BioRob)*. 2012, pp. 282–287.

[118] Ellen M Maathuis et al. “Optimal stimulation settings for CMAP scan registrations”. en. In: *J. Brachial Plex. Peripher. Nerve Inj.* 7.1 (June 2012), p. 4.

[119] Ellen M Maathuis et al. “Reproducibility of the CMAP scan”. en. In: *J. Electromyogr. Kinesiol.* 21.3 (June 2011), pp. 433–437.

[120] Tiago Araújo et al. “Evaluation of Motor Neuron Excitability by CMAP Scanning with Electric Modulated Current”. en. In: *Neurosci J* 2015 (Aug. 2015), p. 360648.

[121] Jordi Badia et al. “Topographical distribution of motor fascicles in the sciatic-tibial nerve of the rat”. In: *Muscle Nerve* 42.2 (2010), pp. 192–201.

[122] Robert I Park. “The bionic eye: retinal prostheses”. en. In: *Int. Ophthalmol. Clin.* 44.4 (2004), pp. 139–154.

[123] Lotfi B Merabet. “Building the bionic eye: an emerging reality and opportunity”. en. In: *Prog. Brain Res.* 192 (2011), pp. 3–15.

[124] Mark S Humayun, Eugene de Juan Jr, and Gislin Dagnelie. “The Bionic Eye: A Quarter Century of Retinal Prosthesis Research and Development”. en. In: *Ophthalmology* 123.10S (Oct. 2016), S89–S97.

[125] Edward Bloch, Yvonne Luo, and Lyndon da Cruz. "Advances in retinal prosthesis systems". en. In: *Ther Adv Ophthalmol* 11 (Jan. 2019), p. 2515841418817501.

[126] D H Hubel and T N Wiesel. "Receptive fields, binocular interaction and functional architecture in the cat's visual cortex". en. In: *J. Physiol.* 160 (Jan. 1962), pp. 106–154.

[127] S G Espinoza, J E Subiabre, and H C Thomas. "Retinotopic organization of striate and extrastriate visual cortex in the golden hamster (Mesocricetus auratus)". en. In: *Biol. Res.* 25.2 (1992), pp. 101–107.

[128] A D Adams and J M Forrester. "The projection of the rat's visual field on the cerebral cortex". en. In: *Q. J. Exp. Physiol. Cogn. Med. Sci.* 53.3 (July 1968), pp. 327–336.

[129] A Santos et al. "Preservation of the inner retina in retinitis pigmentosa. A morphometric analysis". en. In: *Arch. Ophthalmol.* 115.4 (Apr. 1997), pp. 511–515.

[130] M S Humayun et al. "Morphometric analysis of the extramacular retina from postmortem eyes with retinitis pigmentosa". en. In: *Invest. Ophthalmol. Vis. Sci.* 40.1 (Jan. 1999), pp. 143–148.

[131] Yvonne H-L Luo and Lyndon da Cruz. "A review and update on the current status of retinal prostheses (bionic eye)". en. In: *Br. Med. Bull.* 109 (Feb. 2014), pp. 31–44.

[132] Alfred Stett, Andreas Mai, and Thoralf Herrmann. "Retinal charge sensitivity and spatial discrimination obtainable by subretinal implants: key lessons learned from isolated chicken retina". en. In: *J. Neural Eng.* 4.1 (Mar. 2007), S7–16.

[133] Satoru Kawamura and Shuji Tachibanaki. "Rod and cone photoreceptors: molecular basis of the difference in their physiology". en. In: *Comp. Biochem. Physiol. A Mol. Integr. Physiol.* 150.4 (Aug. 2008), pp. 369–377.

[134] V C Smith et al. "Primate horizontal cell dynamics: an analysis of sensitivity regulation in the outer retina". en. In: *J. Neurophysiol.* 85.2 (Feb. 2001), pp. 545–558.

[135] Debarshi Mustafi, Andreas H Engel, and Krzysztof Palczewski. "Structure of cone photoreceptors". en. In: *Prog. Retin. Eye Res.* 28.4 (July 2009), pp. 289–302.

[136] R J Lucas et al. “Regulation of the mammalian pineal by non-rod, non-cone, ocular photoreceptors”. en. In: *Science* 284.5413 (Apr. 1999), pp. 505–507.

[137] Maryam Ghaffari et al. “Chapter 8 - Nanobiomaterials for bionic eye: Vision of the future”. In: *Engineering of Nanobiomaterials*. Ed. by Alexandru Mihai Grumezescu. William Andrew Publishing, Jan. 2016, pp. 257–285.

[138] Hassan A Shah, Sandra R Montezuma, and Joseph F Rizzo 3rd. “In vivo electrical stimulation of rabbit retina: effect of stimulus duration and electrical field orientation”. en. In: *Exp. Eye Res.* 83.2 (Aug. 2006), pp. 247–254.

[139] Consilium Ophthalmologicum Universale. “Visual acuity measurement standard”. In: *Visual Functions Committee* (1984).

[140] S Trauzettel-Klosinski. “Rehabilitation of lesions in the visual pathways”. In: *Klin. Monbl. Augenheilkd.* 226.11 (2009), pp. 897–907.

[141] Marie-Noëlle Delyfer et al. “Adapted Surgical Procedure for Argus II Retinal Implantation: Feasibility, Safety, Efficiency, and Postoperative Anatomic Findings”. en. In: *Ophthalmol Retina* 2.4 (Apr. 2018), pp. 276–287.

[142] Daniel Palanker et al. “Photovoltaic Restoration of Central Vision in Atrophic Age-Related Macular Degeneration”. en. In: *Ophthalmology* (Feb. 2020).

[143] L Hao et al. “Discrimination of multiple PD sources using wavelet decomposition and principal component analysis”. In: *IEEE Trans. Dielectr. Electr. Insul.* 18.5 (Oct. 2011), pp. 1702–1711.

[144] M H Nadian, S Karimimehr, J Doostmohammadi, et al. “A fully automated spike sorting algorithm using t-distributed neighbor embedding and density based clustering”. In: *bioRxiv* (2018).

[145] Daniel N Hill, Samar B Mehta, and David Kleinfeld. “Quality metrics to accompany spike sorting of extracellular signals”. en. In: *J. Neurosci.* 31.24 (June 2011), pp. 8699–8705.

[146] Tom Baden et al. “The functional diversity of retinal ganglion cells in the mouse”. en. In: *Nature* 529.7586 (Jan. 2016), pp. 345–350.

[147] W B Thoreson and J S Ulphani. “Pharmacology of selective and non-selective metabotropic glutamate receptor agonists at L-AP4 receptors in retinal ON bipolar cells”. en. In: *Brain Res.* 676.1 (Apr. 1995), pp. 93–102.

[148] A Stett et al. “Electrical multisite stimulation of the isolated chicken retina”. en. In: *Vision Res.* 40.13 (2000), pp. 1785–1795.

[149] Emilie Mace et al. “Functional ultrasound imaging of the brain: theory and basic principles”. en. In: *IEEE Trans. Ultrason. Ferroelectr. Freq. Control* 60.3 (Mar. 2013), pp. 492–506.

[150] J Salzmann et al. “Subretinal electrode implantation in the P23H rat for chronic stimulations”. en. In: *Br. J. Ophthalmol.* 90.9 (Sept. 2006), pp. 1183–1187.

[151] Marc Gesnik et al. “3D functional ultrasound imaging of the cerebral visual system in rodents”. en. In: *Neuroimage* 149 (Apr. 2017), pp. 267–274.

[152] Sébastien Roux et al. “Probing the functional impact of sub-retinal prosthesis”. en. In: *Elife* 5 (Aug. 2016).

[153] Olivier Macherey and Robert P Carlyon. “Cochlear implants”. en. In: *Curr. Biol.* 24.18 (Sept. 2014), R878–R884.

[154] Marwan Hariz. “Twenty-five years of deep brain stimulation: celebrations and apprehensions”. In: *Mov. Disord.* 27.7 (2012), pp. 930–933.

[155] Xiao Yang et al. “Bioinspired neuron-like electronics”. In: *Nat. Mater.* (2019).

[156] Kostas Kostarelos et al. “Graphene in the Design and Engineering of Next-Generation Neural Interfaces”. en. In: *Adv. Mater.* 29.42 (Nov. 2017).

[157] Alice T Chuang, Curtis E Margo, and Paul B Greenberg. “Retinal implants: a systematic review”. en. In: *Br. J. Ophthalmol.* 98.7 (July 2014), pp. 852–856.

[158] Jennifer Goode. “Use of International Standard ISO 10993-1,‘Biological evaluation of medical devices-Part 1: Evaluation and testing within a risk management process’”. In: *Department of Health and Human Services Food and Drug Administration* 68 (2016).

[159] Freeman J Dyson. *Imagined Worlds*. en. Harvard University Press, 1998.

[160] Yuval Noah Harari. *21 Lessons for the 21st Century*. en. Random House, Aug. 2018.

[161] Giovanni Miano and Antonio Maffucci. *Transmission Lines and Lumped Circuits: Fundamentals and Applications*. en. Elsevier, Feb. 2001.